



Article

OC, HPC, UHPC and UHPFRC Corrosion Performance in the Marine Environment

Josep Ramon Lliso-Ferrando ^{1,2,*}, José Manuel Gandía-Romero ^{1,2} , Juan Soto ¹ and Manuel Valcuende ² 

¹ Research Institute for Molecular Recognition and Technological Development (IDM), Universitat Politècnica de València, Camino de Vera, s/n., 46022 Valencia, Spain

² Department of Architectural Constructions, School of Architecture, Universitat Politècnica de València, Camino de Vera, s/n., 46022 Valencia, Spain

* Correspondence: jollife2@arq.upv.es

Abstract: This work aims to study the corrosion performance of six concretes in the marine environment: three ordinary concretes (C30, C40 and C50); one high-performance concrete (C90); two ultra high-performance concretes, one without fibres (C150-NF) and another one with steel fibres (C150-F). To this end, porosity and chloride ingress resistance were analysed at different ages. Resistivity was also evaluated and the corrosion rate in the embedded rebars was monitored. The results showed that C30, C40 and C50 had porosity accessible to water percentages and capillary absorption values between six- and eight-fold higher than C90 and C150-NF and C150-F, respectively. Similar differences were obtained when oxygen permeability was analysed. Chloride ingress resistance in the ordinary concretes was estimated to be one-fold lower than in C90 and two-fold lower than in C150-NF and C150-F. Presence of fibres in C150-F increased the diffusion coefficient between 5% and 50% compared to C150-NF. Fibres also affected resistivity: C150-NF had values above 5500 Ωm , but the C150-F and C90 values were between 700 and 1000 Ωm and were one-fold higher than the ordinary concretes. After 3 years, the corrosion damage in the embedded rebars exposed to a marine environment was negligible in C90, C150-NF and C150-F (9.5, 6.2 and 3.5 mg mass loss), but with higher values (between 170.4 and 328.9 mg) for C3, C40 and C50. The results allow a framework to be established to make comparisons in future studies.

Keywords: reinforced concrete structures; corrosion; marine environment; chloride diffusion; resistivity; porosity



Citation: Lliso-Ferrando, J.R.; Gandía-Romero, J.M.; Soto, J.; Valcuende, M. OC, HPC, UHPC and UHPFRC Corrosion Performance in the Marine Environment. *Buildings* **2023**, *13*, 2439. <https://doi.org/10.3390/buildings13102439>

Academic Editors: Youyou Zhang, Qing Sun, Yang Zhang and Lu Ke

Received: 23 August 2023

Revised: 18 September 2023

Accepted: 22 September 2023

Published: 25 September 2023



Copyright: © 2023 by the authors. Licensee MDPI, Basel, Switzerland. This article is an open access article distributed under the terms and conditions of the Creative Commons Attribution (CC BY) license (<https://creativecommons.org/licenses/by/4.0/>).

1. Introduction

Today, second only to water, concrete is the most consumed material in the world [1], and is also the most used construction material worldwide [2,3]. At present, around 7.5×10^9 cubic meters of concrete are made each year [4]. Such mass consumption is due to its main advantages: its strength and mechanical properties, its versatility and adaptability [5], its abundant availability [6] and the low cost of raw materials [7]. Another property that distinguishes reinforced concrete from other building materials is its durability. This term refers to materials' ability to withstand aggressive environmental actions, and to maintain performance well above a minimum acceptable level during its service life with no undue serviceability loss or the need for major repairs [8,9]. Among the different causes of reinforced concrete structures' (RCS) premature damage, corrosion of reinforcement is the predominant and most crucial deteriorating mechanism [10], especially when RCS are located in marine environments [11–14]. This process gradually affects RCSs' service life and their performance [15].

The relation between time and RCS deterioration due to corrosion phenomena is well known. As defined by Tuutti in 1982 [16], two scenarios are considered. On the one hand, the initiation stage, when aggressive agent (CO_2 and chlorides) ingress occurs within concrete up to rebars, which results in the progressive disruption of the passive

layer on the steel surface and triggers corrosion onset. This results in the second scenario, the propagation stage, when the average corrosion rate rises, but not linearly because it is affected by environmental factors like temperature or humidity. The appearance of cracks also influences this evolution and accelerates degradation up to a maximum level of tolerated damage. Consequently, RCS performance progressively worsens and reaches unacceptable minimums [15] (Figure 1).

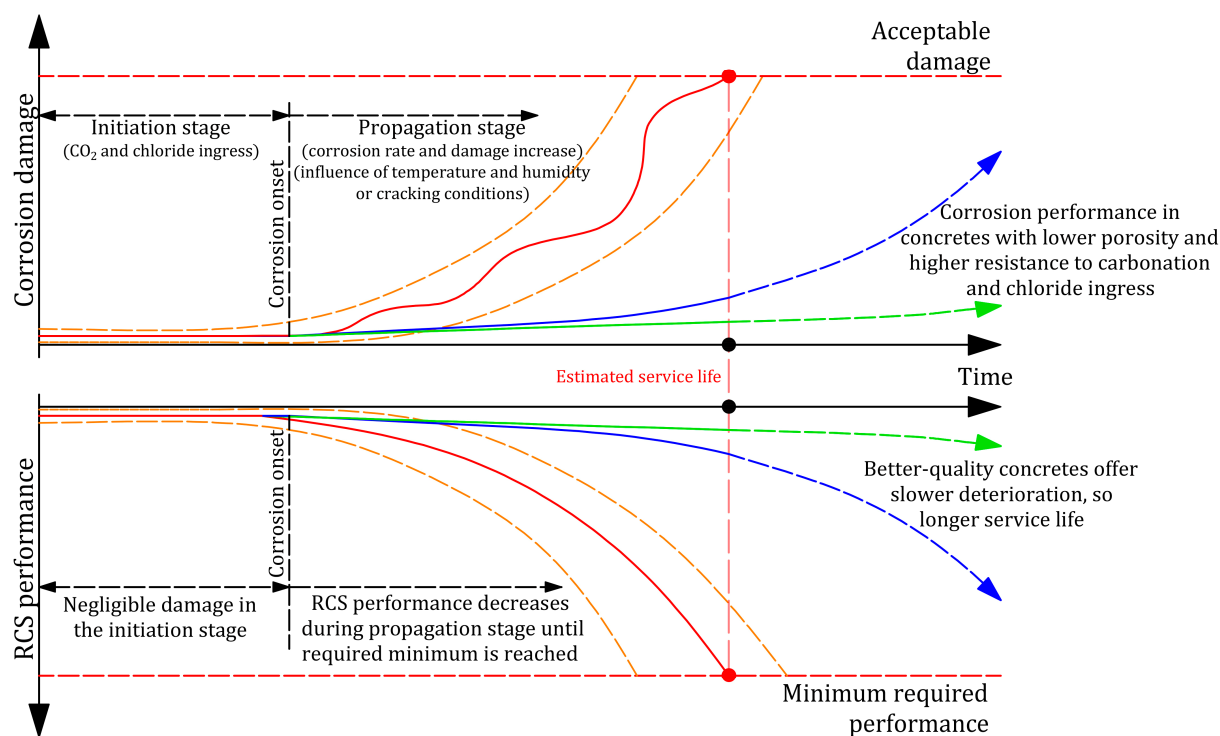


Figure 1. Schematic representation of corrosion damage and RCS performance according to time.

To fight this, and to minimise corrosion damage in RCS, especially those located in marine environments, some authors have proposed using corrosion-resistant reinforcements like stainless steel [17–20] or fibre-reinforced polymer bars [21], such as those made of carbon fibre [22,23] or glass fibre [24,25]. Nonetheless, carbon steel is irreplaceable due to the practical advantages of low cost, easy field processing, versatility and mechanical performance [13,26]. This situation means having to focus on improving concrete quality to guarantee better steel protection. For RCS in marine environments, this refers to refining the porous structure, reducing their permeability to water and gas, and also increasing resistance to chloride diffusion, which are decisive actions [26] (Figure 1).

In such a context, and as an alternative to ordinary concrete (OC), high-performance concrete (HPC) started being developed in the 1970s. As reported by ACI 363-R, HPC might range from 83 to 103 MPa compressive strength, despite 55 to 62 MPa are already being produced commercially as HPC [27]. HPC mixtures are generally characterised by including supplementary materials, such as silica fume, and using low water/binder (w/b) ratios (0.25–0.4) [27]. A maximum aggregate size of 13 mm is recommended, and large quantities of superplasticiser are also used to achieve accurate workability [28]. In this way, very compact mixes are obtained that not only improve the material's mechanical performance, but also enhance the durability of this concrete type [29]. Many works have focused on analysing the mechanical properties of HPC, such as those that focus on compressive strength and fracture energy [30], strength and modulus of elasticity [31], abrasion resistance [32], split tensile strength [33] or pulse velocity and Poisson's ratio [34]. In contrast, works that have analysed aspects related to the durability and corrosion performance of these materials are scarcer. Some authors have studied this by centring on

analysing the porosity of HPC given its close relation to permeability, and resistance to the diffusion of corrosion precursor agents like chlorides. For instance, Bharatkumar et al. [35] obtained porosity accessible to water (PAW) percentages between 7.33% and 8.95% in their mixes, while Poon et al. [36] reported similar results (between 7.05% and 8.35%). Both these works indicated lower results than the reference values (12–14%) considered for OCs [37]. Conversely, studying other parameters also related to HPC durability, such as the oxygen permeability test, provided much more disperse results. Khan and Lynsdale [38] obtained an oxygen permeability coefficient (K_{ox}) at 28 days of between 1 and $3 \times 10^{-17} \text{ m}^2$. However, Shi et al. [39,40] and Zhang et al. [41] indicated higher and more disperse values of between 1 and $16 \times 10^{-17} \text{ m}^2$ and 15 and $35 \times 10^{-17} \text{ m}^2$. The large differences in the results obtained by several authors are repeated in studies that have analysed other durability-related properties, for instance, the chloride diffusion coefficient. Ozawa et al. [42] found values close to $2.5 \times 10^{-12} \text{ m}^2/\text{s}$ by means of EPMA (electron probe microanalysis). Conversely, Song and Kwon [43] reported values between 0.5 and $2.2 \times 10^{-12} \text{ m}^2/\text{s}$ in line with Standard ASTM C1202-12 [44]. Other authors have followed Standard NT-Build 492 [45], and also obtained widely dispersed results: between 2.8 and $4.6 \times 10^{-12} \text{ m}^2/\text{s}$ [46], 2.12 and $3.23 \times 10^{-12} \text{ m}^2/\text{s}$ [47] or 8 and $8.5 \times 10^{-12} \text{ m}^2/\text{s}$ [48]. These data prove how difficult it is to compare different works and to reveal the improvements of HPC compared to OCs. The reason for all this is the broad casuistry in each study, such as the variety of mixtures or different testing methods. Furthermore, other studies that have centred on HPC durability have compared the influence of curing conditions [49] or high-temperature treatments at early ages [50–53]. Some authors' works have studied the impact of introducing recycled aggregates into mixes [54,55], or additions, such as rice husk [56–58], industrial waste [59] or ceramic waste [60]. In all these cases, comparisons have been made using an HPC base and the variants that each author proposes, which also prevents making comparisons to other works or to OCs.

In order to face new durability requirements, ultra high-performance concrete (UHPC) appeared later in the 1990s [61]. As defined by some authors, this new material can be described as the combination of HPC and self-compacting concrete (SCC) [62]. The French recommendation [63] defined this material with a characteristic compressive strength higher than 150 MPa, but also affirmed that UHPC can be considered as such when exceeding 120–130 MPa [64]. The mixtures applied when manufacturing this material are characterised by w/b ratios below 0.3. Coarse aggregates are eliminated, and the maximum sand size is limited to 15–60 mm to obtain much more homogeneous mixes. As some authors also point out [65], not only must these limitations be taken into account, but so should a careful selection of materials with suitable physicochemical properties. For this purpose, adding silica fume [66–68], blast furnace slag [69,70], fly ash [71–73], quartz powder [74], granite powder [68] or glass powder [75,76] is usual. With these new mixes, it is possible to generate extremely dense matrices with very low porosity and permeability, as some authors have demonstrated [61]. For example, Liu et al. [61] defined total porosity to be 8.2% for UHPC using MIP testing at 28 days, which was slightly higher than the results presented by Valcuende et al. [77] or Tuan et al. [78] with 7.3% and 7.5%. Nonetheless with tests performed at 90 days, Abdulkareem et al. [79] obtained values of between 2.51% and 4.81%, which are practically half those reported in other works (6.95%) [78]. Other authors have reported values between 1% and 2% [71,80,81] when UHPC was heat-treated [81,82]. The results found in the literature about the oxygen permeability of UHPC are less disperse than they are for HPC. Wang et al. [83] reported a K_{ox} coefficient of $0.8 \times 10^{-19} \text{ m}^2$. Tafroui et al. [84] and Ghafari et al. [85] presented similar results with 1.5×10^{-19} and $2.5 \times 10^{-19} \text{ m}^2$. In any case, the obtained results reveal lower porosity than HPC, which is also reflected in good chloride diffusion resistance. For instance, authors like Matos et al. [86] estimated a chloride diffusion coefficient of $1.99 \times 10^{-12} \text{ m}^2/\text{s}$ on average by migration tests run on the UHPCs that they prepared [45]. This value coincides with the results that other authors have presented [87–89], whose ranges were between 1.77 and $2.12 \times 10^{-12} \text{ m}^2/\text{s}$, 1.11 and $1.50 \times 10^{-12} \text{ m}^2/\text{s}$ and 1.50 and $2.00 \times 10^{-12} \text{ m}^2/\text{s}$.

In other cases however, lower values have been reported and range from $0.83 \text{ m}^2/\text{s}$ [90] to $2.00 \times 10^{-14} \text{ m}^2/\text{s}$ [71], which once again demonstrates the very disperse results in the literature. Nevertheless, some authors coincide in pointing out that UHPCs are more brittle than HPC [91–93], which results in poor crack propagation resistance.

Including steel fibres in UHPC significantly improves the ductility of these concretes [94–97] and maintains good resistance to compression (above 120 and up to 150 MPa) [98–102]. This new type of mix is defined as ultra high-performance fibre-reinforced concrete (UHPCFRC). The optimum percentage of fibres pointed out by several authors to prepare this new generation of cementitious materials goes from 0.5% to 2% in volume [103,104], but some authors also suggest that this percentage can reach 5% [105]. Despite this increase slightly improving some properties like flexural strength [105], it comes with a much higher economic cost than when limiting contents to 2% [106]. Although these new concretes were developed no more than 20 years ago, several authors have demonstrated the improvements they offer according to different durability-related properties. For example, Abushanab et al. [107] and Pyo and Kim [70] indicated PAW percentages of between 0.86% and 3.41% and 2% and 4%. Some authors who have analysed K_{ox} coefficient present average values of 1.4×10^{-18} [108] and $7.7 \times 10^{-18} \text{ m}^2$ [109], and even lower ones with 1.0×10^{-19} in some cases [77,110]. These values are lower than in HPC and similar to UHPC, which denotes certain data dispersion. Once again, the differences in the analysed mixtures, curing conditions or the standard test methodology make it difficult to compare several works. This comes over quite clearly when, for example, comparing the results in the literature about chloride diffusion in UHPCFRC, which are analysed mainly using accelerated testing like NT-Build 492 [45]. Some values vary between 4.74 and $6.63 \times 10^{-12} \text{ m}^2/\text{s}$ [77] or 1.1 and $1.4 \times 10^{-13} \text{ m}^2/\text{s}$ [102]. Despite these differences, the results in all cases are at the thresholds for which very low or practically negligible chloride diffusion can be considered (threshold of $1 \times 10^{-12} \text{ m}^2/\text{s}$ [109]).

These data reveal how structures produced with UHPC or UHPCFRC can offer better corrosion performance, especially in marine environments. However, the ample casuistry that appears in the literature regarding tests or applied mixes, and the fact that no works have cross-sectionally performed a comparative study that goes from Ocs ($f_c \approx 30 \text{ Mpa}$) to concretes with resistance close to 150 Mpa , makes simple comparisons difficult. To this end, the present work aims to study the corrosion performance of six concretes in the marine environment: three ordinary concretes (C30, C40 and C50); one high-performance concrete (C90); two ultra high-performance concretes, one without fibres (C150-NF) and another one with steel fibres (C150-F). The properties of each mix were analysed from three points of view. On the one hand, concrete porosity (porosity accessible to water, capillary suction coefficient and gas permeability) at different ages. On the other hand, the chloride diffusion resistance was estimated for each concrete. For this purpose, the non-steady chloride diffusion coefficient was determined using a migration test and a unidirectional diffusion test. Concrete resistivity was also studied. From the third point of view, the corrosion of the reinforced test specimens prepared with these concretes and exposed to marine conditions was monitored for more than 3 years. Visual inspection was performed at the end of this study.

2. Experimental Plan

2.1. Materials

Six different concretes were produced: three Ocs (a low-strength concrete (C30), a medium-strength concrete (C40) and a high-strength concrete (C50)); one HPC concrete (C90); one UHPC (C150-NF); and one UHPCFRC (C150-F). To manufacture all the concretes, cement CEM I 42.5 R/SR was used, except for concrete C30, for which CEM II 32.5 B-L was employed (both from LAFARGE). In Ocs, sand (0/4) and limestone gravel (4/12) were utilised. In concretes C50 and C90, sand (0/4) and limestone gravel (4/7) were used. For UHPC and UHPCFRC, coarse aggregates were replaced with a studied mix of fine silica sands: fine sand 0/0.5 and medium sand 0.6/1.2. The C90 mixture included silica fume from Elkem, while the C150-NF and C150-F contained silica fume (Elkem) and silica flour

(Sibelco Quarzfin US-500). Into C150-F, steel fibres (\varnothing 0.2 mm and 13 mm length) were also incorporated with 2% content in relation to the total concrete volume. To manufacture all the concretes, superplasticiser Sika[®] ViscoCrete[®]-20HE was employed. Table 1 shows the characteristics of each mix. Table 1 includes the water/binder (w/b) ratios. This parameter relates the weight of water and the weight of cement and supplementary particles (silica fume) in each mixture. Table 1 also includes the average compressive strength (f_c) of each concrete type at different ages (3, 7 and 28 days; 2, 6 and 12 months) by experiments run on nine cylindrical specimens (\varnothing 100 mm; height 200 mm). Three batches from each mix were made and three samples per batch were analysed. All the manufactured samples of each concrete type were moist-cured for 28 days at 20 ± 2 °C and relative humidity (RH) higher than 95%. At the end of the curing period, all the samples were stored under laboratory conditions (23 ± 2 °C and $65 \pm 10\%$ RH) until the corresponding test age.

Table 1. Mixture proportions of concrete (kg/m³ concrete).

	C30	C40	C50	C90	C150-NF	C150-F
CEM II 32.5, B-L	307	-	-	-	-	-
CEM I 42.5, R-SR	-	292	450	500	800	800
Water	184	190	225	178	160	160
Superplasticiser	1.85	2.80	1.37	3.50	30	30
Silica fume	-	-	-	55	175	175
Silica flour	-	-	-	-	225	225
Limestone sand (0/0.5)	-	-	-	-	302	302
Limestone sand (0.6/1.2)	-	-	-	-	565	565
Limestone sand (0/4)	1438	1256	880	914	-	-
Limestone gravel (4/7)	-	-	880	779	-	-
Limestone gravel (4/12)	491	707	-	-	-	-
Steel fibres (\varnothing 2 × 13 mm)	-	-	-	-	-	175
w/b ¹ ratio	0.60	0.65	0.50	0.32	0.16	0.16
f_c (3 days)	19.51	23.49	26.77	63.92	98.29	81.02
f_c (7 days)	25.40	32.20	35.31	70.15	118.64	112.45
f_c (28 days)	30.67	39.47	51.75	88.86	129.76	135.43
f_c (2 months)	31.88	41.23	48.14	94.45	161.05	145.72
f_c (1 year)	30.11	38.78	47.93	85.67	151.96	148.23

¹ Water/binder ratio. F_c : compressive strength (Mpa).

2.2. Test Methods

Corrosion is the main cause of deterioration in reinforced concrete structures located in marine environments. This phenomenon is indirectly related to concrete's resistance to aggressive agents ingress, as chlorides, which is, in turn, related to the material's porosity [111]. Furthermore, the kinetic of corrosion processes is related to the oxygen availability in the reinforcement and the material's resistivity. Both water and oxygen are the main oxidant agents involved in the reduction–oxidation reaction of rebar corrosion [112]. Accordingly, and in order to analyse the performance of each presented concrete, a series of tests was carried out. The concrete porosity of each mix was analysed by determining the porosity accessible to water and the capillary absorption coefficient. The oxygen permeability of each mix was also determined because it is a closely related parameter to the size of pores, their connectivity, and the tortuosity of the path. The chloride ingress resistance of each concrete was analysed using a chloride migration test and a chloride diffusion test. An electrical resistance test was also performed. Finally, a monitoring process was followed of the corrosion in the rebars embedded in the samples produced with each concrete described in Section 2.1, which were exposed to a marine environment (partially immersed in seawater) for 1095 days. At the end of the exposure period, a visual rebar inspection and an SEM analysis were performed.

2.2.1. Porosity Accessible to Water

Porosity accessible to water (PAW) was determined as specified in Standard UNE 83980:2014 [113]. This test was performed at the ages of 28 days and 2, 6 and 12 months on $100 \times 100 \times 50 \text{ mm}^3$ prismatic specimens. Before testing, specimens were oven-dried at $105 \text{ }^\circ\text{C}$ to constant weight (M_{dry}). Then they were vacuum-dried in a chamber at a pressure lower than 2.0 kPa. For 2 h, they were left under these conditions. Afterwards, the chamber was filled with water to a height of 20–30 mm on specimens. After 24 h, specimens were removed from the chamber and the hydrostatic (M_{hyd}) and postvacuum saturated mass (M_{sat}) were found. PAW was determined from the formula depicted in the standard (Equation (1)). Three batches from each mix were made and three samples per batch were analysed. The result of each mix was taken to be the arithmetic mean of the nine recorded values.

$$\text{Porosity accessible to water(\%)} = 100 \times \frac{(M_{\text{sat}} - M_{\text{dry}})}{(M_{\text{sat}} - M_{\text{hyd}})} \quad (1)$$

2.2.2. Capillary Absorption Coefficient

The capillary absorption coefficient (K) was determined as indicated in Standard UNE-EN 83982:2008 [114]. This test was also performed at the ages of 28 days and 2, 6 and 12 months on $100 \times 100 \times 50 \text{ mm}^3$ prismatic specimens. The test specimens were conditioned as depicted in UNE-EN 83966:2008 [115]. Once specimens had been conditioned, the K coefficient was determined by following up variation in the mass of the samples in contact with a water lamina of $5 \pm 1 \text{ mm}$. This process was applied until the samples' mass became stable (when the difference in weights between two separate weighing sessions within a minimum 24 h period was below 0.1%). The K value was obtained with the equations described in the standard [114]. Three batches from each mix were made and three samples per batch were analysed. The result of each mix was taken to be the arithmetic mean of the nine recorded values.

2.2.3. Oxygen Permeability Coefficient

The oxygen permeability coefficient (K_{ox}) was determined using Standard UNE 83981:2008 [116] at the ages of 28 days and 2, 6 and 12 months on cylindrical samples ($\varnothing 150 \text{ mm}$ and 50 mm height). The side surfaces of all the test specimens were epoxy-coated prior to testing to prevent oxygen release. Later specimens were oven-dried at $50 \text{ }^\circ\text{C}$ for 4 days and stored for 24 h in a desiccator for cooling, as depicted in the standard [116]. Once the conditioning process ended, tests were performed in a permeability cell filled with synthetic air as depicted in Figure 2. Oxygen permeability was analysed at five air pressure settings (1.2, 2, 2.5, 3 and 3.5 bar) in a Controls permeameter (model 58-E0031). Air flow was taken by measuring the time it took a soap bubble to travel through a glass tube of a known volume (in this case: 10 cm^3 , 25 cm^3 and 100 cm^3). $K_{\text{ox,p}}$ was obtained according to Equation (2) depending on the test pressure:

$$K_{\text{ox,p}} = \frac{1.14 \times 10^{-4} \times Q \times p_a}{(p^2 - p_a^2)} \quad (2)$$

where atmospheric pressure (p_a) and test pressure (p) are expressed as N/m^2 and the gas flow that passes the sample (Q) is expressed as m^2/s . As testing was conducted at different pressures, the K_{ox} value for each sample was obtained by taking the average of the distinct values obtained for each tested pressure. Three batches from each mix were made and three samples per batch were analysed. The result of each mix was taken to be the arithmetic mean of the nine recorded values.

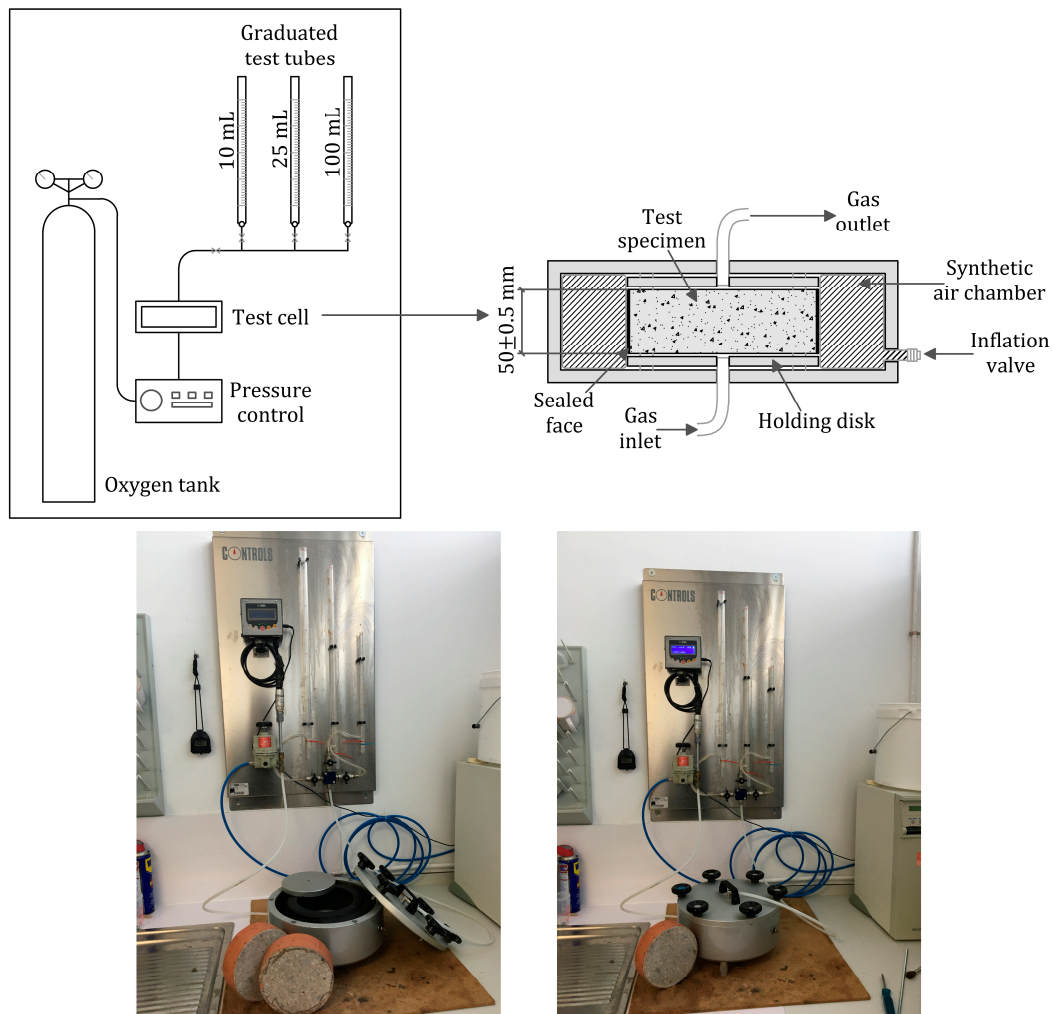


Figure 2. Setup for the oxygen permeability test.

2.2.4. Chloride Migration Coefficient

The chloride migration coefficient from the non-steady state migration experiment (D_{nssm}) was determined in accordance with Standard UNE-EN 12390-18:2021 [117]. Cylindrical specimens were used (\varnothing 100 mm and 50 mm height) and tests were performed at the ages of 28 days and 2, 6 and 12 months. The side surfaces of all the specimens were epoxy-coated prior to testing as indicated in the standard [117]. Later, they were vacuum-saturated with calcium hydroxide 24 h before testing. For tests, specimens were placed in a cell as depicted in Figure 3. One side was exposed to a 2-molar chloride solution and the other side to a 0.3-molar sodium hydroxide solution. Then a potential difference was applied between both specimen sides to force chloride migration through concrete. The value of the applied potential difference and test duration was determined according to the previously performed calibration by applying a potential difference of 30 V as the test standard points out [117]. After testing, each specimen was taken out from the measuring cell and axially split. Inner surfaces were sprayed with silver nitrate solution (0.1 M AgNO_3), and chloride-polluted areas were indicated by a whitish colour. This enabled the penetration depth to be measured. Then, the chloride migration coefficient was determined according to the expression set out in the standard (Equation (3)):

$$D_{nssm} = \frac{0.0239 \times T \times L}{(U - 2) \times t} \times \left(x_d - 0.0238 \times \sqrt{\frac{T \times L \times x_d}{(U - 2)}} \right) \quad (3)$$

where the following are considered: temperature in Kelvin grades (T); test duration in hours (t); sample thickness in mm (L); the value of the applied voltage in volts (U). Parameter x_d corresponds to the mean value of chloride penetration in mm in the sample, obtained using the analysis performed with silver nitrate. Three batches from each mix were made and three samples per batch were analysed. The result of each mix was taken to be the arithmetic mean of the nine recorded values.

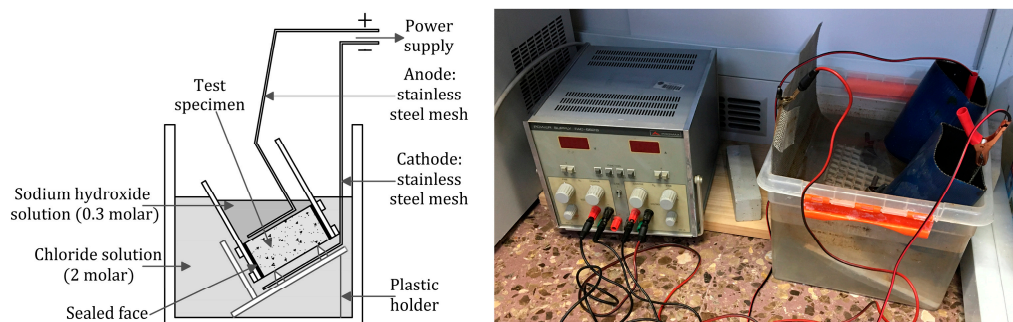


Figure 3. Setup for the chloride migration test.

2.2.5. Chloride Diffusion Coefficient

Chloride diffusion can also be determined using a non-accelerated test. In this case, the chloride diffusion coefficient from the non-steady state or apparent diffusion coefficient (D_{app}) was determined as depicted in Standard UNE-EN 12390-11:2019 [118]. This test was performed at the age of 28 days on cylindrical specimens (\varnothing 100 mm and 100 mm height). Prior to testing, specimens were epoxy-coated (except for the exposed face). Once the painting had dried, specimens were vacuum-dried in a chamber at a pressure between 1.0 and 5.0 kPa, where they remained for 3 h. Afterwards, the chamber was filled with demineralised water. After 24 h, the test specimens were removed from the vacuum chamber. Upon an uncoated surface, a water tank (300 mm high) filled with 0.5 M chloride solution was placed. Specimens were left under these conditions for 90 days as indicated in the standard [118]. After this time, a chloride analysis was performed on drilled-out samples obtained at different depths according to UNE-EN 14629:2007 [119]. Figure 4 shows some pictures of this process. Three batches from each mix were made and two samples per batch were analysed. The result of each mix was taken to be the arithmetic mean of the six recorded values.



Figure 4. Setup for the chloride diffusion test and the chloride analysis.

2.2.6. Concrete Resistivity

Concrete resistivity is another parameter that plays a key role in embedded rebar corrosion [120] because this material property refers to resistance to electric charge displacement. When rebar depassivation occurs, electrons are displaced through metal, where electrical resistance is practically unnoticeable. This process also requires ions to move through the concrete matrix. In this circuit, concrete's resistance to ionic movement is that which controls corrosion process kinetics [121,122]. Concrete resistivity was determined according to Standard UNE-EN 83988-1:2008 [123] on prismatic specimens ($40 \times 40 \times 160 \text{ mm}^3$). Once the curing process had finished, the two specimen ends were cut to remove the concrete layer cover in the area where the electrodes were placed because this layer was richer in

cement than the rest of the specimen owing to the wall effect that occurs during casting in the areas in contact with formworks [124,125]. Later test specimens were vacuum-dried in a chamber at a pressure lower than 0.15 kPa. They remained under these conditions for 3 h. Afterwards, the chamber was filled with demineralised water. After 24 h, specimens were removed, they were surface-dried with a damp cloth and conductivity I was determined by applying a uniform electric field using two flat stainless-steel electrodes ($40 \times 40 \text{ mm}^2$) that came into contact with specimens' bases. To ensure good electrical contact between electrodes and specimens, some previously dampened sponges of the same area as the electrodes were placed. To ensure that the applied pressure was homogeneous, a press with two nylon plates and metal bars was used. Measurements were taken with a commercial conductivity meter (model Crison GLP 32) (Figure 5). The value was recorded 1 min after measurements commenced to ensure that the recorded signal was stable enough. Concrete resistivity (ρ_e in Ωm) was obtained according to Equation (4):

$$\rho_e = \frac{S}{L} \times R_e \quad (4)$$

where S and L correspond to the area and edge of samples (in meters), respectively; R_e (in Ω) corresponds to concrete's electrical resistance, obtained with the measured inverse of conductivity (in Siemens) ($R_e = 1/C$). After the first measurement, all the samples were immersed in water for more than 1 year. The measuring process was periodically repeated to know the evolution of this parameter in each concrete type. Three batches from each mix were made and three samples per batch were analysed. The result of each mix was taken to be the arithmetic mean of the nine recorded values.

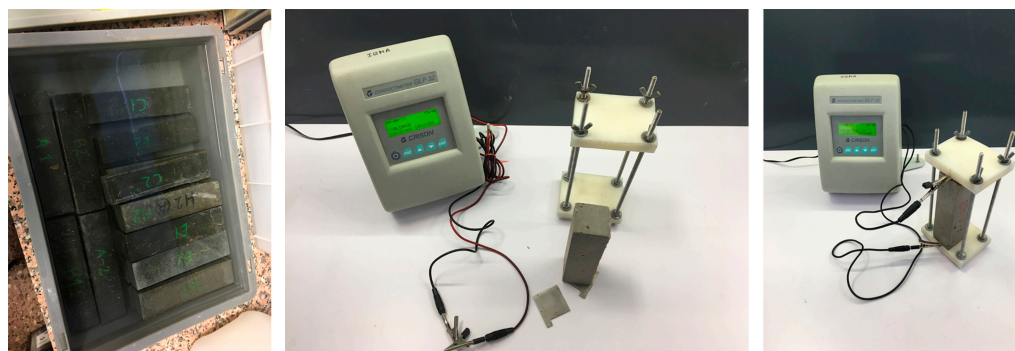


Figure 5. Setup for the concrete resistivity test.

2.2.7. Corrosion Rate

The corrosion rate analysis was performed on the rebars (B 500 SD, \varnothing 10 mm and 100 mm long) embedded in the cylindrical test specimens (\varnothing 50 mm and 100 mm height) as depicted in Figure 6. As observed, rebars were partially protected with a PVC pipe filled with epoxy painting. The surface area in contact with concrete was delimited to 50 mm^2 (1571 mm^2). The end of the bar was used for electrical contact purposes while taking measurements, and it was protected with Vaseline to prevent corrosion. After the curing period (at the age of 28 days), the top of the specimens was epoxy-coated. They were later partially immersed (up to 75%) in 0.5 M sodium chloride solution, which was prepared according to ASTM D1141-98 (2021) [126]. The exposure condition lasted for more than 3 years. Three batches from each mix were made and four samples per batch were analysed. The result of each mix was taken to be the arithmetic mean of the 12 recorded values.

During the exposure period, the corrosion rate was periodically measured in each rebar using the potentiostatic step voltammetry (PSV) technique. This technique has been described and validated in previous works [127–130]. It allows for rebar corrosion analysis by studying the response of steel to potentiostatic-type disturbance. The PSV method has been used in other studies [131,132], and is also employed for corrosion monitoring systems in RCS [133]. In this case, measurements were taken with an Autolab PGSTAT

100 Potentiostat. The Nova 1.11 software was used for signal processing. The measuring cell arrangement was a 3-electrode one: the working electrode (WE) on which corrosion was measured was each rebar; a stainless-steel piece, partially immersed in solution, was used as a counter electrode (CE); a saturated calomel electrode (SCE, model Radiometer Analytical XR110), partly immersed in solution, was employed as the reference electrode (RE), as depicted in Figure 7. Having determined corrosion intensity, it was normalised by the rebar surface being in contact with concrete to obtain i_{CORR} . Later, the corrosion rate was determined according to Equation (5):

$$V_{CORR} = 0.0116 \times i_{CORR} \tag{5}$$

where V_{CORR} is expressed as mm/year and i_{CORR} as $\mu A/cm^2$.

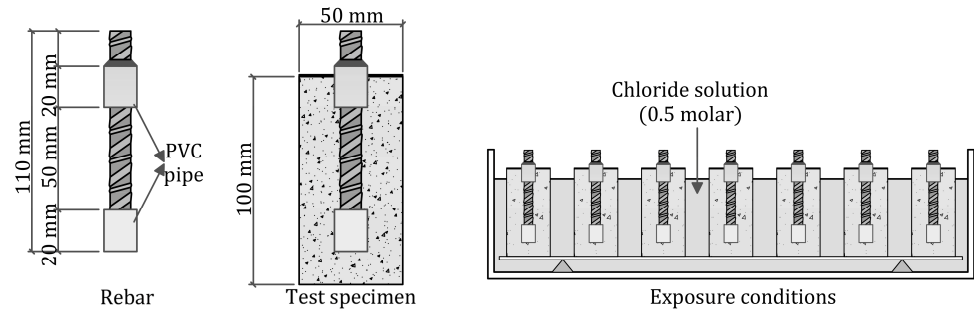


Figure 6. Test specimens used for the corrosion rate tests and the exposure conditions.

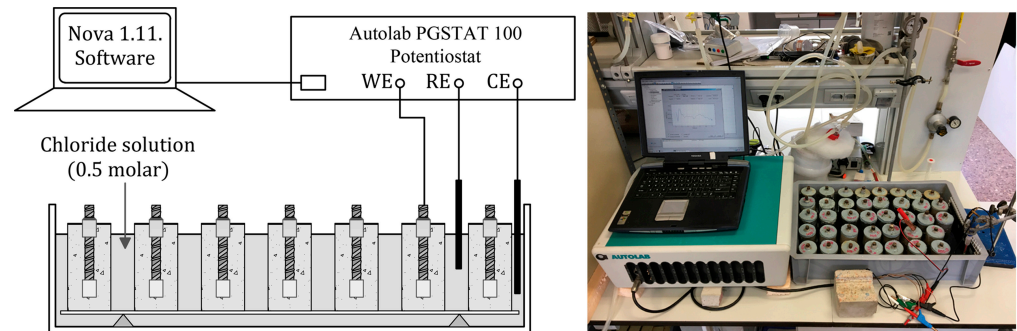


Figure 7. Setup for the corrosion rate measurements.

3. Results

3.1. Porosity Accessible to Water

The average PAW percentage was obtained per test age and for each concrete type, as seen in Figure 8.

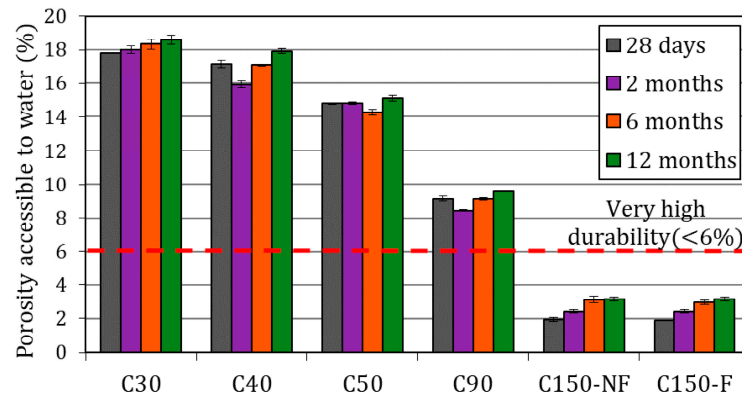


Figure 8. Porosity accessible to water.

The PAW in UH concretes (C150-NF and C150-F) ranged between 2% and 3%, below the threshold to be considered as very high durability concretes (<6%) [37]. These results were 75% lower than those obtained in the C90, and almost one order of magnitude lower than the C50 (14–15%) and the C30 and C40 concretes, where the results ranged between 16% and 19%. The HPC and UHPC were less porous than the rest due to the applied doses: a lower water/cementitious material ratio (<0.32), as well as a more homogenous mix given the maximum size of the employed aggregates. Different authors have proven that, apart from these details, including silica fume in mixes allows for lowering the percentage of pores in hardened concrete, and results in porous structures with greater tortuosity [134–137]. This phenomenon means lesser pore interconnection, which significantly limits water permeability, as the obtained results reveal.

Regarding the influence of fibres in UHPCs, no statistically significant differences were observed between concretes C150-NF and C150-F. These results confirm the MIP findings obtained in previous tests [77], according to which variation in fibre content between 0–2% does not affect the porous structure of UHPC (total pore volume and pore size distribution are similar).

3.2. Capillary Absorption Coefficient

The capillary absorption coefficient (K) obtained for each concrete type and for all the testing ages appears in Figure 9.

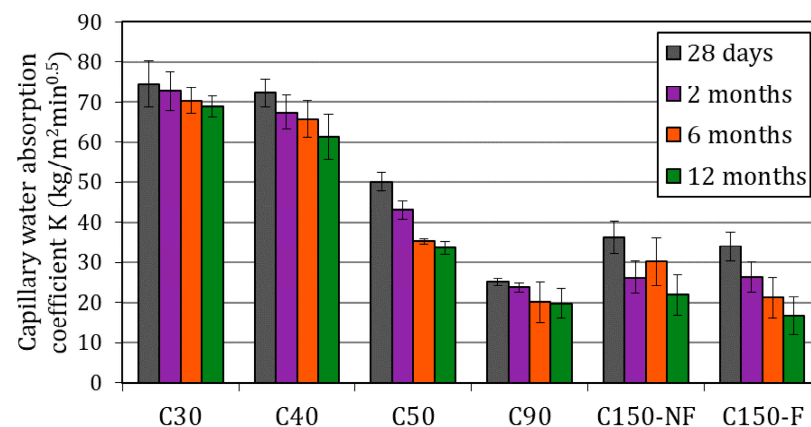


Figure 9. Capillary water absorption.

The obtained results indicate a similar tendency to that noted during the PAW test. Concretes C30 and C40 were the materials from which higher coefficients were obtained, which were between 40% and 50% higher than for C50. However, the difference between C50 and the better performing concretes (C90, C150-NF and C150-F) was not significant (between 10% and 30%). Moreover, the differences among them (C90, C150-NF and C150-F) were virtually non-existent, and a K coefficient between 16 and 36 kg/m² min^{0.5} was obtained in all cases. This similarity among the obtained values came from the mathematical formulation used to obtain the K coefficient described in the standard [114]. In the case of very low permeability concretes (as C90, C150-F and C150-NF), the saturation time of the specimens is very low, since, as has been proven in previous work using MIP tests, the pore size is very small and the porous network is segmented [77]. Because of all this, the equation given in the standard for obtaining the K coefficient provides misleading results (Equation (6)):

$$K = \frac{\delta_w \times \left(\frac{Q_n - Q_0}{A \times h \times \delta_w} \right)}{10 \times \sqrt{\frac{t_n}{h^2}}} \quad (6)$$

where δ_w is water density (1 g/cm³), coefficient Q_n and coefficient Q_0 correspond to samples' weight upon saturation and the initial pretest weight (in g), respectively, and

values A and h refer to the area and edge of the analysed sample (in cm). This coefficient is inversely proportional to the saturation time expressed as mins (t_n) and therefore tends to infinity since t_n is practically zero. Due to this, in this work, another parameter was chosen to analyse the capillary porosity of this type of concrete: the increase in weight per unit area ($\Delta P/A$). This parameter is similar to that proposed by other standards [138], and is obtained from the difference in weight between the weight at saturation (Q_n) and the initial weight (Q_0), divided by the area of the test specimen (A) (Equation (7)):

$$\Delta P/A = \frac{(Q_n - Q_0)}{A} \quad (7)$$

The analysis of this coefficient allowed for establishing clear differences among the distinct tested concrete types, above all for concretes C90, C150-NF and C150-F (Figure 10).

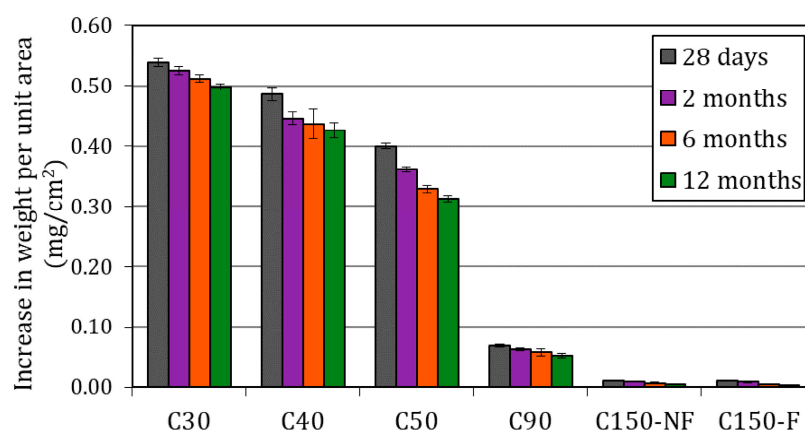


Figure 10. Increase in weight per unit area.

The results obtained from studying the weight increase per surface unit ($\Delta P/A$) indicated that values were five-fold lower in concretes C150-NF and C150-F versus C90. As in the PAW test, the use of fibre did not influence the capillary absorption of the UHPCs. The average result in the UHPCs ranged between 0.010 and 0.004 mg/cm². Yet, other authors [86], who analysed the same parameter following [139], reported an average value of 1.4 mg/cm². In this case, conditioning was performed by drying at 40 °C, and not inside a chamber at 20 °C and 65% RH, which had an influence by leading to a significant increase in capillary absorption. Furthermore, the results obtained for the samples made with concrete C50 were six-fold higher than those obtained with C90. These data are more closely related to those found in the PAW test and revealed the suitability of using this parameter for more adequately analysing concrete's capillary absorption capacity.

Another conclusion drawn from analysing this parameter was concretes' different evolution over time. In all cases, reduced capillary absorption was noted from the first test at 28 days, and the rest at 2, 6 and 12 months. The differences in the results between the tests at 28 days and 1 year in concretes C30, C40 and C50 were 8%, 14% and 28%, and were 32%, 114% and 173% for C90, C150-NF and C150-F, both respectively. This logical evolution corresponded to the continuous cement hydration process with time, and this phenomenon gradually reduces capillary absorption. These differences were bigger in the concretes with a lower w/b ratio (C150-NF and C150-F) and were, therefore, those with a higher non hydrated cement content after mixing.

3.3. Oxygen Permeability Coefficient

The oxygen permeability coefficients (K_{ox}) obtained at each test age and per concrete type appear in Figure 11.

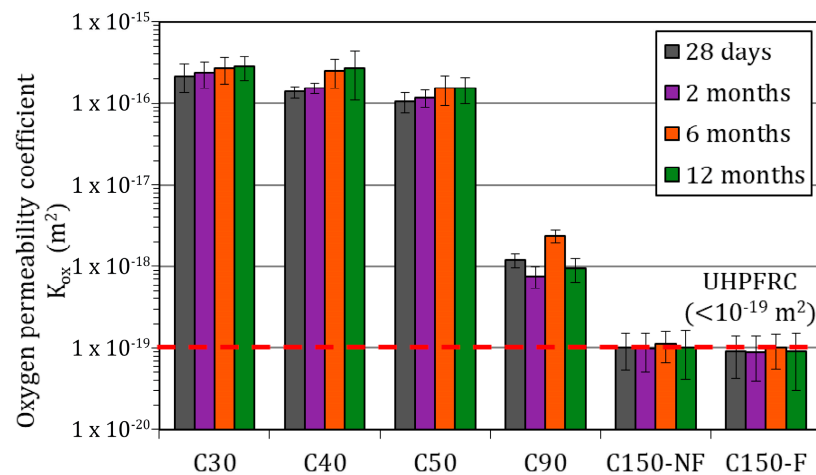


Figure 11. Oxygen permeability coefficient.

The oxygen permeability coefficient data were like the results of the previously presented tests. Ocs (C30, C40 and C50) had values that were more than two orders of magnitude over that for C90 and three orders of magnitude more than for C150-NF and C150-F. The average values obtained for UHPFCs were slightly below 10^{-19} m^2 , which is the threshold set by the French Civil Engineering Association to define UHPFRC permeability [138]. This same recommendation also establishes that the threshold at which concrete can be considered very high-performance concrete (VHPC) is 10^{-18} m^2 , which is a similar value to that obtained for C90, which is herein considered to be HPC.

The importance of studying this parameter lies in the fact that it is a good indirect indicator of concrete durability. The reinforcement corrosion rate is associated with O_2 availability in the cementitious matrix [112]. These results, along with those obtained from the PAW and capillary absorption tests, allowed for the properties of the concretes' porosity to be clearly differentiated.

3.4. Chloride Migration Coefficient

The influence of concretes' porosity on chloride penetration was studied using accelerated testing (by migration) and unidirectional diffusion testing. In the former, penetration occurred due to the potential difference, but the latter was caused by a chloride concentration gradient. Figure 12 provides the results of the chloride migration coefficient in the non-steady state (D_{nssm}) obtained for each concrete and per test age.

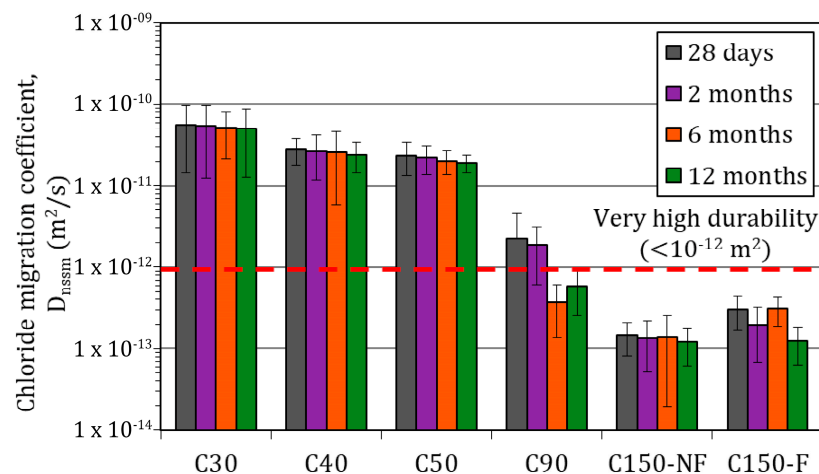


Figure 12. Chloride migration coefficient.

As the results show, there is a close relation between these data and those obtained when PAW, capillary suction coefficient or oxygen permeability were analysed. In this case, the values for the Ocs (C30, C40 and C50) varied between 6×10^{-11} and $2 \times 10^{-11} \text{ m}^2/\text{s}$, which was more than one order of magnitude compared to C90. The values of UH concretes (C150-NF and C150-F) were two orders of magnitude lower, and came close to $1 \times 10^{-13} \text{ m}^2/\text{s}$, which was below the limit set by other authors ($1 \times 10^{-12} \text{ m}^2/\text{s}$) for concrete to be considered to have very high durability [37]. Authors like Hooton et al. [140], Byfors [141] or Torii et al. [142] have also identified the drop in chloride diffusion in concrete that takes place when silica fume is added to mixes. This is owing to the change that occurs in gel CSH due to such action, which reduces porosity, above all in the aggregate–cementitious matrix transition, and also increases porous network tortuosity. Other authors have even demonstrated this using electron probe microanalysis [143,144]. In addition, due to the high cement content used in C90, C150-NF and C150-F, the C_3A content is high. This cement compound reacts with chlorides to form calcium chloroaluminates. So, the content of free chlorides in concrete is lower.

During the porosity analysis, it was impossible to establish clear differences between concretes C150-NF and C150-F. Conversely, differences were noted when analysing chloride penetration resistance. The obtained results indicated D_{nssm} to be between 5% and 50% higher when steel fibres were included in mixes (C150-F). Other authors have also reported this situation for accelerated chloride diffusion tests using UHPCs with and without fibres [145–149]. Some studies point out that the interfacial transition zone of steel fibres and the cementitious matrix is weaker (higher porosity) than that of aggregates and the cementitious matrix, which slightly favours chloride penetration compared to mixes to which no fibres are added [150]. Furthermore, the existence of fibres can lead to the formation of fibre balls with pores inside them [151–153]. Nevertheless, the values obtained in both concretes (C150-NF and C150-F) were well below the threshold set out for very high durability ($1 \times 10^{-12} \text{ m}^2/\text{s}$) [37].

3.5. Chloride Diffusion Coefficient

The chloride content of each of the samples extracted from the specimens exposed for 90 days to a 3% NaCl solution is presented in Figure 13.

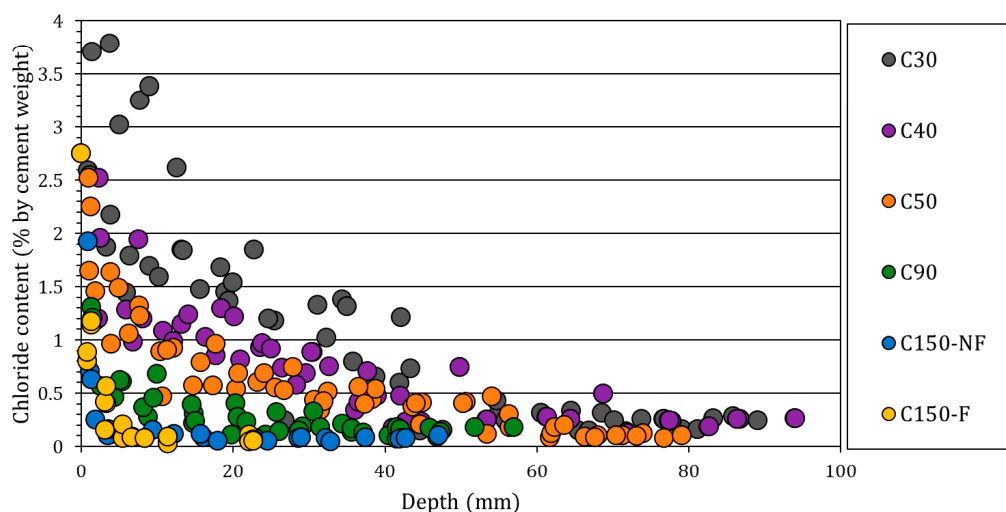


Figure 13. Chloride penetration profiles.

Both the followed standard [118] and the studies performed by different authors [115,154–156] indicate that chloride diffusion in concrete is governed by Fick's second law of diffusion. Thus, for a given chloride content in relation to a given cement I weight (expressed as %) at a certain depth (x) in meters and for an exposure period (t)

in seconds, it is possible to calculate the D_{app} coefficient (expressed as m^2/s) according to Equation (8):

$$C_{(x,t)} = C_0 + (C_s - C_0) \times \left[1 - \operatorname{erf}\left(\frac{x}{2 \times \sqrt{D_{app} \times t}}\right) \right] \quad (8)$$

where the error function is:

$$\operatorname{erf}(z) = \frac{2}{\sqrt{\pi}} \times \int_0^z e^{-u^2} du \quad (9)$$

Parameters C_s and C_0 correspond to chloride content, expressed as % in relation to the cement weight on the surface and before testing began. The C_0 value was obtained after analysing the specimens not contaminated by chloride exposure. The obtained values were 0.03% for concretes C150-F and C150-NF, 0.04% for C90, and 0.09% for concretes C30, C40 and C50. This content corresponds to that introduced by the raw materials used to manufacture concretes.

The chloride content values on the surface (C_s) and the diffusion coefficient in a non-steady state (D_{app}) were obtained using least squares fitting in Equation (8) and the experimental data of the chloride content at different depths are presented in Figure 13. Figure 14 shows the D_{app} value obtained in each concrete using the experimental data.

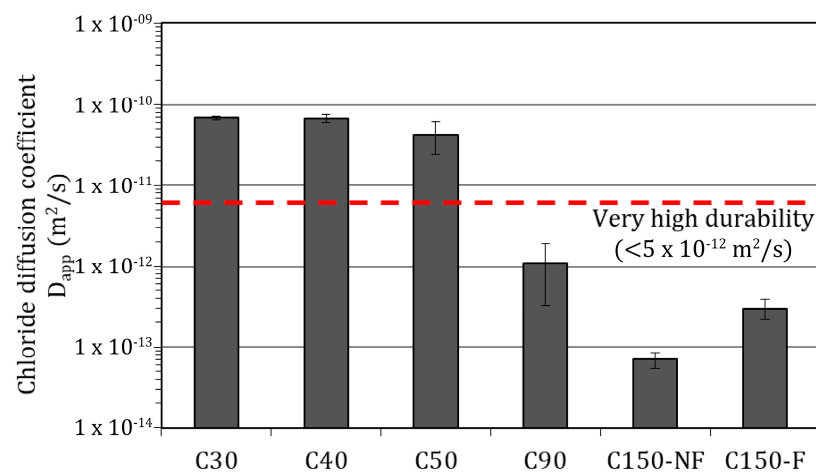


Figure 14. Chloride diffusion coefficient.

The values obtained for concretes C30, C40 and C50 were between 6.9×10^{-11} and $4.3 \times 10^{-11} m^2/s$. In concrete C90, D_{app} was $1.1 \times 10^{-12} m^2/s$, which was more than one order of magnitude lower. Regarding the UHPCs, the value for C150-F was $3.0 \times 10^{-13} m^2/s$, with $6.9 \times 10^{-14} m^2/s$ for C150-NF, which are four-fold lower. The tendency in the obtained results was similar to that noted in the accelerated migration test. However, authors like Andrade [157] have demonstrated that comparing both testing methods is unsuitable because they involve different diffusion processes.

Notwithstanding, D_{app} is a good indicator of the durability of concrete. Obtaining this parameter allows for estimations to be made of the time needed for chlorides to reach rebars at a given depth (concrete cover) and in a critical quantity (C_{crit}) to trigger corrosion onset under similar exposure conditions to those in the test. For this purpose, by considering the D_{app} , C_0 and C_s data acquired from the tests performed on each concrete type, and for a known cover ($x = 0.02$ m, corresponding to the cover of the specimens described in Section 2.2.7), it is possible to deduce chloride content evolution (expressed as % by cement weight) ($C_{(0.02,t)}$) according to time. This is shown in Equation (10), obtained from Equation (8):

$$C_{(0.02,t)} = C_0 + (C_s - C_0) \times \left[1 - \operatorname{erf} \left(\frac{0.02}{2 \times \sqrt{D_{\text{app}} \times t}} \right) \right] \quad (10)$$

Figure 15 shows chloride content evolution in relation to time for a 20 mm cover according to the analysed concrete type.

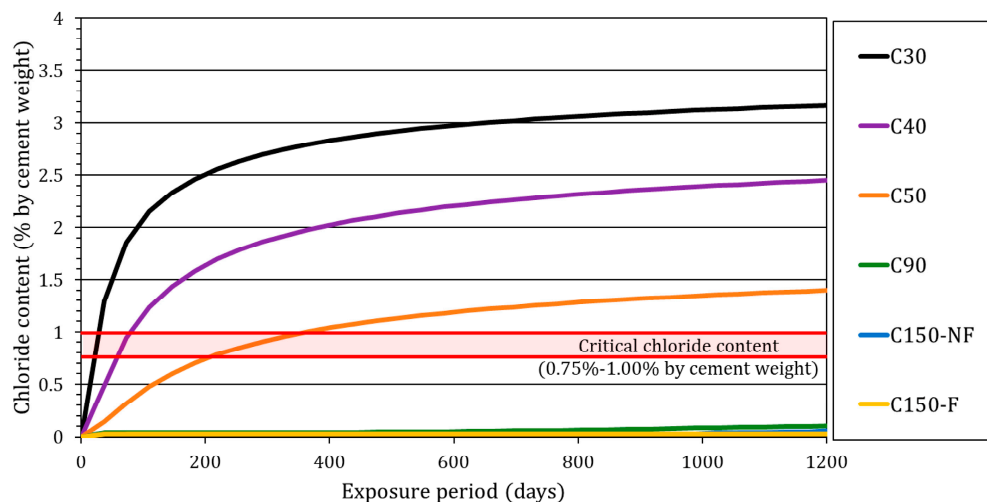


Figure 15. Chloride content evolution according to exposure time at a 20 mm cover depth.

The critical chloride content for corrosion onset (C_{crit}) to occur is an extensively studied value. In the last 50 years, a considerable amount of papers with values for it has been published [14,158]. However, no specific value for this parameter is found in the literature. The different study conditions of each work or the methodology used to determine it mean that the literature contains a wide range of proposed values, with values scattering over two orders of magnitude according to [158]. Given this situation, many authors take a value of $C_{\text{crit}} = 1\%$ chloride content by cement weight to make estimations [159]. Accordingly, the graph in Figure 15 shows the interval from 0.75% to 1.00% of chloride content in relation to cement weight as a threshold at which rebar depassivation takes place. This has served to forecast the estimated period for corrosion onset to occur in each concrete when considering a 20 mm cover. For concretes C90, C150-NF and C150F, the intersection between the obtained curves and the threshold from 0.75% to 1.00% chloride content by cement weight was much superior to the period study (3 years). Conversely with concretes C30, C40 and C50, the time estimated during which corrosion onset would occur was 36, 75 and 255 days, respectively.

3.6. Concrete Resistivity

Figure 16 shows the resistivity evolution during the monitoring process for the specimens described in Section 2.2.6.

Once again, the obtained results evidenced large differences between the Ocs (C30, C40 and C50) and HPC/UHPCs (C90, C150-NF and C150-F). The increased permeability in the porous network led to greater conductivity and a reduction in the material's electrical resistance. Throughout practically the entire monitoring period, the values obtained for concrete C30 were 30% lower than those obtained in C40 and C50, which coincides with the results found in previous tests. Furthermore, the differences between C40 and C50 at the end of the monitoring period were 8–10%.

The results obtained in concretes C90 and C150-F indicated similar values: between 750 and 1050 Ωm . These values came close to the threshold of 1000 Ωm established by Baroghel-Bouny [37] to consider durability to be very high, and denotes a negligible corrosion risk. According to the water absorption and capillary absorption tests, this is attributable to much lower water porosity. However, a large difference was found between

concretes C150-NF and C150-F. With UHPC, to which no steel fibres were added, values exceeded $5500 \Omega\text{m}$, which were five-fold those obtained with the same concrete, but to which steel fibres had been added. These data indicate that steel fibres increase material's conductivity because steel has negligible resistance to electrons' movement, so they act as linkage bridges between pores. As a result, fibre content increases, and they provide the shortcut for the ionic current to flow more easily. Martinie et al. [160] also indicated the influence of using small prismatic specimens in this test because of the fibre alignment that takes place, which contributes to increased conductivity. In any case, although fibres significantly reduce concrete's resistivity, the inclusion of steel fibres does not prevent the reference values that denote very high durability from being obtained.

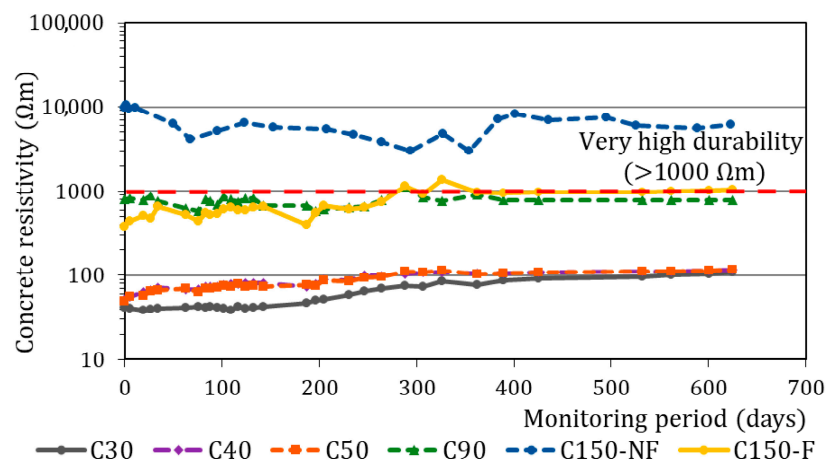


Figure 16. Resistivity evolution.

3.7. Corrosion Rate

For more than 3 years, follow-up was conducted of the corrosion rate of the 72 embedded rebars in the six concrete types (12 samples per concrete type). Figure 17 shows the average corrosion rate (V_{CORR}) of the rebars embedded in the specimens partially immersed in chloride solution. This figure also depicts the thresholds considered in Standard UNE 112072:2011 [161] to set the corrosion level according to V_{CORR} values: $V_{\text{CORR}} < 1 \mu\text{m}/\text{year}$, negligible corrosion; $1 < V_{\text{CORR}} < 5 \mu\text{m}/\text{year}$, low corrosion; $5 < V_{\text{CORR}} < 10 \mu\text{m}/\text{year}$, moderate corrosion; $V_{\text{CORR}} > 10 \mu\text{m}/\text{year}$, high corrosion.

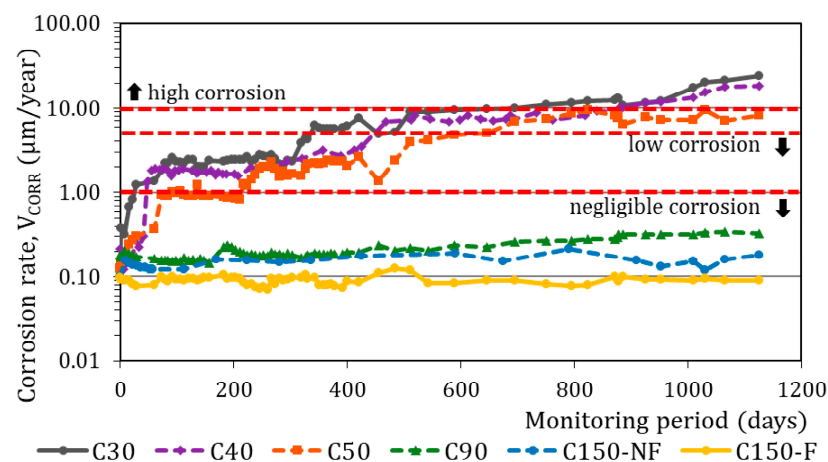


Figure 17. The obtained corrosion rate values.

For the first weeks, the corrosion rate values obtained in all the rebars were below $1 \mu\text{m}/\text{year}$, which is the set threshold for considering a negligible corrosion level. This trend continued throughout the entire period for the UHPCs (C150-F and C150-NF). The

values at the end of the monitoring period were 0.18 and 0.09 $\mu\text{m}/\text{year}$, respectively. For concrete C90, slightly higher corrosion levels were noted than for UHPC (from one- to three-fold higher). In any case, corrosion remained below 0.33 $\mu\text{m}/\text{year}$ at the end of the monitoring period. These results coincide with the estimations found in Section 3.5, where the depassivation of the embedded rebars was not expected in any of these three concretes when considering the concrete cover (20 mm) and the study period (3 years).

The corrosion evolution in the OCs (C30, C40 and C50) was completely different. Between 40 and 380 exposure days, corrosion increased in the rebars embedded in the three concretes with values over 1 $\mu\text{m}/\text{year}$. In C30, this increase occurred on exposure day 35. In concrete C40, values were over 1 $\mu\text{m}/\text{year}$ as of 60 exposure days. In C50, the increase took place as of 227 days. These data also coincide with the estimations made using the unidirectional chloride diffusion test presented in Section 3.5 (Figure 15). When the monitoring period finished (after 1095 exposure days), the corrosion rate in concretes C30, C40 and C50 was 24.4, 18.3 and 8.2 $\mu\text{m}/\text{year}$, respectively.

These results demonstrate the corrosion performance of each concrete. However, to quantify and compare each studied mixture, accumulated damage must be analysed. To do so, by integrating the corrosion rate–time curve, the mass loss (Δm_{loss}) that accumulated during the exposure period was calculated in accordance with Faraday's law (Equation (11)) as shown by:

$$\Delta m_{\text{loss}} = \frac{M}{n \times F} \times \int_{V_{\text{CORR},0}}^{V_{\text{CORR}}} \frac{V_{\text{CORR}}}{0.0116} \times dt \quad (11)$$

where M is the steel atomic mass (55.845 g/mol), t is the time in seconds, n is the number of electrons released or acquired during the corrosion process (two for this case) and F is Faraday's constant (96,845 C/mol). Mass loss (Δm_{loss}) was obtained as g/cm^2 and normalised by rebars' working area (1571 mm^2). Figure 18 presents the obtained Δm_{loss} results.

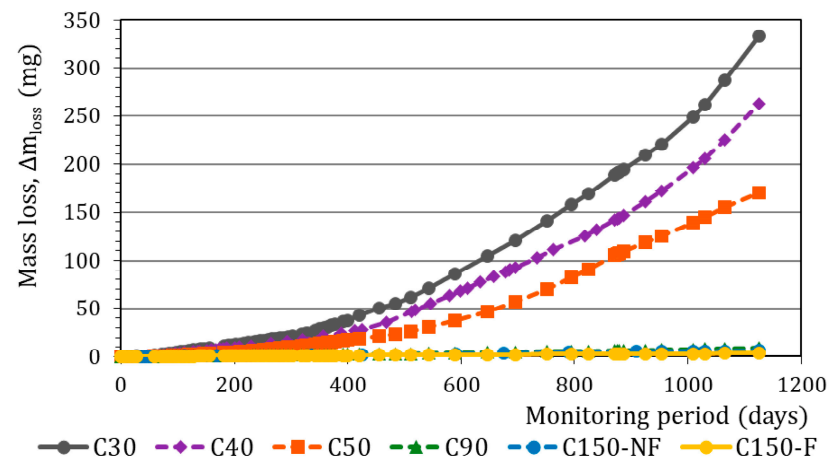


Figure 18. Estimated mass loss.

According to Equation (11), the accumulated mass loss in concretes C90, C150-NF and C150-F was 9.5, 6.2 and 3.5 mg, respectively. These values can be considered negligible values compared to those obtained for Ocs. For C30, the average accumulated mass loss was 328.9 mg, 267.9 mg for C40 and 170.4 mg for C50. The excellent corrosion behaviour of HPC, and mainly of UHPC, is due to their good resistance to chloride diffusion (no depassivation took place during the whole study period, with $V_{\text{CORR}} < 1 \mu\text{m}/\text{year}$), to their high resistivity (ionic current intensity is much lower) and probably also to very low oxygen availability (with an oxygen permeability coefficient between two and three orders of magnitude lower). Conversely in Ocs, mass loss for the first weeks was slight (<10 mg in all cases at 200 days). After 200 days however, an abrupt change in tendency occurred and coincided with rebar depassivation.

At the end of the exposure period, several samples of each concrete type were visually inspected. On their surfaces, small microcracks were observed on the samples manufactured with Ocs (Figure 19). No damage was visually noticed in samples C90, C150-NF and C150-F. Superficial corrosion was only detected for the fibres in C150-F, but it had not spread to inner fibres. Then, rebars were removed from specimens and were cleaned as described in ASTM G1-03 [162]. Figure 19 shows the state that rebars were in after this process. Figure 20 shows two SEM images of a rebar embedded in C50 with a moderate corrosion level and another embedded in C30 with high corrosion level.



Figure 19. Test specimen inspection.

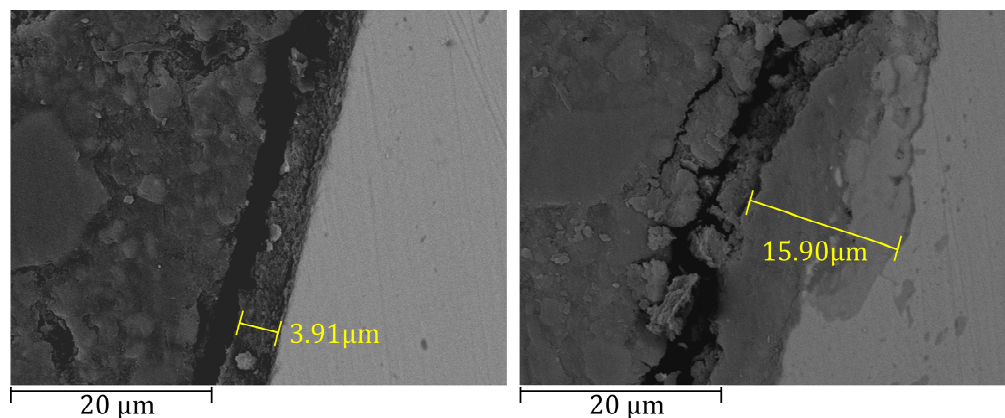


Figure 20. SEM images.

The visual rebars inspection revealed pitting on the specimens embedded in concretes C30 and C40. No apparent damage was observed for those embedded in C50. Despite obtaining values over 1 µm/year, no pitting due to the incipient corrosion state occurred. No damage was noticed for the rebars embedded in concretes C90, C150-NF and C150-F, which coincides with the data acquired during monitoring periods.

By means of the SEM images, the formation of mixed oxide layers was identified, where mainly ferric oxide (Fe_2O_3) and ferrous ferric oxide (Fe_3O_4) were found. The average thickness obtained in reinforcement with a moderate corrosion level was less than 4 micrometres. In the rebar embedded in C30, where the corrosion level was high, pits were found and the oxide layer thickness in some areas was three-fold greater and exceed 15 micrometres.

3.8. Summary of the Results

Figure 21 shows the results of the tests performed for the different concrete types at 28 days, except for the resistivity tests, for which the last value obtained at the end of the monitoring period was taken; and the corrosion rate study, which considered the average mass loss estimated at the end of the exposure period. As the baseline (value = 100), the results obtained for the samples manufactured with C90 for each test were employed. The graph included variations (%) in the results obtained for the other concrete types in the semilogarithmic scale. This representation allows the improvements or limitations of some concretes versus others to be graphically noted.

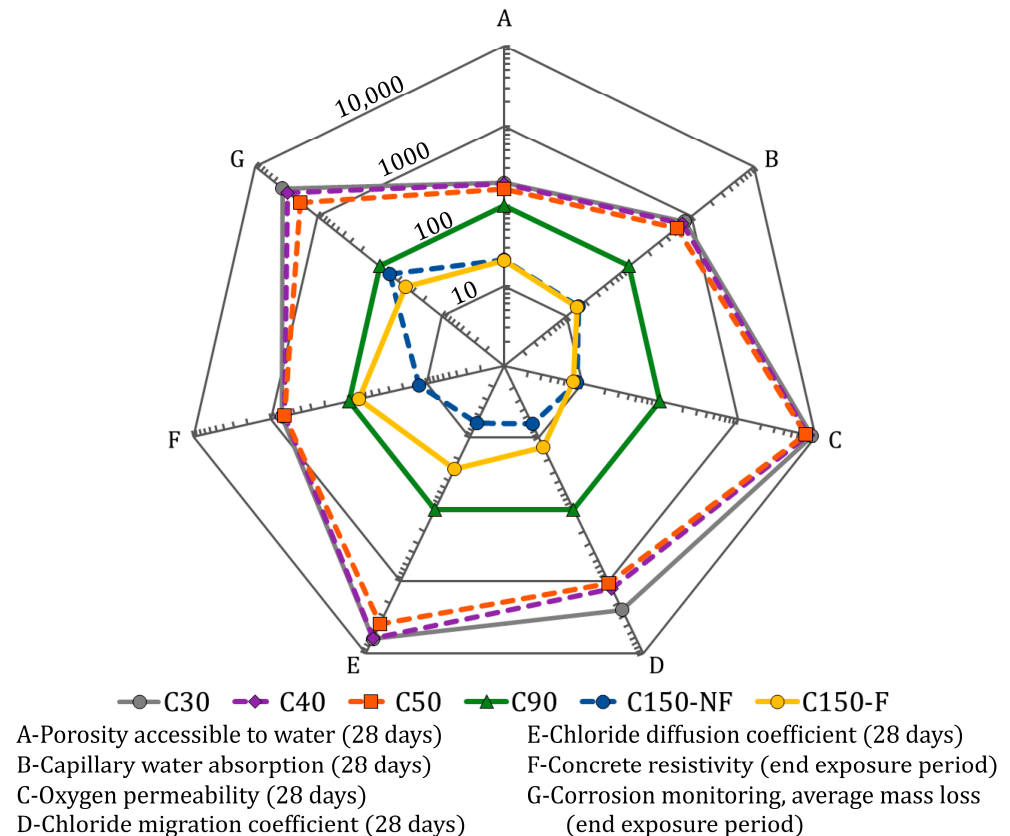


Figure 21. Comparing the results.

As the comparative graph shows, in all the parameters analysed in Ocs, a significantly more limited response was noted than for HPC (C90). In some cases, the difference was more than one order of magnitude, as with the oxygen permeability or the chloride resistance (migration and diffusion) tests. In other cases, variation was slighter as in the PAW analysis, the capillary absorption test, or the resistivity study. The differences for Ocs were scarce, particularly in the porosity analyses. Conversely, in other tests, such as chloride diffusion resistance or resistivity, differences were larger and C50 offered the best response. This situation meant better performance for C50 in the corrosion rate study about the embedded rebars, in which depassivation took place later than in those embedded in C30 and C40. Consequently, the accumulated mass loss in the rebars in C50 was 63% and 51% lower than in the rebars in C30 and C40, respectively.

Moreover, the UHPCs (C150-F and C150-NF) offered a slightly better response than C90. In both cases, the maximum aggregate size was limited to 1.2 mm, and the w/b ratio was lower than it was for C90 (0.32 vs. 0.13). This led to mixes being more homogeneous and with less porosity than HPC. In the tests that centred on the porosity analysis (PAW, capillary absorption, and oxygen permeability), the obtained results were one order of magnitude lower in C150-NF and C150-F than in C90. The differences between both

UHPCs in these studies were minimum. Conversely, the chloride migration, unidirectional chloride diffusion and resistivity tests revealed a better response for C150-NF than for C150-F. Additionally, the presence of metal fibres increases a material's ion conductivity. This resulted in lower electrical resistance for C150-F versus C150-NF (six-fold lower at the end of the study period). On the contrary, when the response of both concretes was analysed using the corrosion analysis in the embedded rebars, the average mass loss after over 3 years of exposure to a marine environment was 3.4 mg and 6.2 mg, expressed as C150-F and C150-NF, respectively. In both these concretes and C90, mass loss was negligible because it was between one order and two orders of magnitude lower than in the OCs.

4. Conclusions

This work analysed the corrosion performance of six different concretes in a marine environment: three ordinary concretes (C30, C40 and C50); one high-performance concrete (C90); and two ultra high-performance concretes, one without fibres (C150-NF) and the other reinforced with steel fibres with 2% content of the total concrete volume (C150-F). The obtained results allowed for the following conclusions to be reached:

1. In the HPC and UHPCs, water absorption and capillary absorption were between six- and eight-fold lower than in OCs. In addition, the oxygen permeability coefficient was two and three orders of magnitude lower in HPC and in UHPCs, respectively;
2. The non-steady state migration coefficient (D_{nssm}) and the apparent diffusion coefficient (D_{app}) were one order of magnitude lower than for OCs. The values obtained for concretes C150-F and C150-NF were almost two orders of magnitude lower, but due to the steel fibres, the resistance to chloride penetration was somewhat lower in C150-F than in C150-NF. In any case, the values obtained in both concretes were well below the threshold for very high durability ($1 \times 10^{-12} \text{ m}^2/\text{s}$);
3. Resistivity analysis evidenced differences among concretes. Ordinary concretes (C30, C40 and C50) showed values close to $100 \Omega\text{m}$. Conversely C90 and C150-F reached values that were almost one order of magnitude higher. In addition, a large difference between concretes C150-NF and C150-F was found. With UHPC, to which no steel fibres were added, values exceeded $5500 \Omega\text{m}$, which were five-fold those obtained with the same concrete, but to which steel fibres had been added. These data indicate steel fibres increase material's conductivity and significantly reduce concrete's resistivity. In any case, however, steel fibres do not prevent the reference values denoting very high durability from being obtained;
4. The corrosion rates of the rebars embedded in OCs after being exposed to a marine environment for more than 3 years were high ($>10 \mu\text{m}/\text{year}$). In HPC, UHPC and UHPFRC, corrosion was negligible ($<1 \mu\text{m}/\text{year}$). Regarding accumulated damage, the mass loss estimated at the end of the study in the rebars embedded in C90, C150-NF and C150-F was, respectively, 9.5, 6.2 and 3.5 mg. On the contrary, the values obtained with OCs were two orders of magnitude higher: 328.9, 267.9 and 170.4 mg in C30, C40 and C50, respectively.

This study demonstrates the corrosion performance of each concrete type exposed to a marine environment and allows for a framework to be established to make comparisons in future studies.

Author Contributions: Conceptualisation, J.R.L.-F. and M.V.; methodology, M.V.; software, J.R.L.-F.; validation, J.R.L.-F., J.M.G.-R., J.S. and M.V.; formal analysis, J.R.L.-F.; investigation, J.R.L.-F. and M.V.; resources, J.M.G.-R., J.S. and M.V.; data curation, J.R.L.-F.; writing—original draft preparation, J.R.L.-F.; writing—review and editing, J.R.L.-F., J.M.G.-R., J.S. and M.V.; visualisation, J.R.L.-F., J.M.G.-R., J.S. and M.V.; supervision, J.M.G.-R., J.S. and M.V.; project administration, J.M.G.-R., J.S. and M.V.; funding acquisition, J.M.G.-R., J.S. and M.V. All authors have read and agreed to the published version of the manuscript.

Funding: This research was funded by the Spanish Government, grant number PID2020-119744RB-C21 funded by MCIN/AEI/10.13039/501100011033.

Data Availability Statement: The data presented in this study are available upon request from the corresponding author.

Acknowledgments: The authors thank the Spanish Government for grant PID2020-119744RB-C21 funded by MCIN/AEI/10.13039/501100011033, and the support of the Universitat Politècnica de València. They are also grateful for the predoctoral scholarship granted to Josep Ramon Lliso Ferrando as part of the “Formación de Personal Investigador” programme from the Universitat Politècnica de València (FPI-UPV-2018).

Conflicts of Interest: The authors declare no conflict of interest.

References

1. Gagg, C.R. Cement and concrete as an engineering material: An historic appraisal and case study analysis. *Eng. Fail. Anal.* **2014**, *40*, 114–140. [[CrossRef](#)]
2. Angst, U.M. Challenges and opportunities in corrosion of steel in concrete. *Mater. Struct. Constr.* **2018**, *51*, 4. [[CrossRef](#)]
3. Flatt, R.J.; Roussel, N.; Cheeseman, C.R. Concrete: An eco material that needs to be improved. *J. Eur. Ceram. Soc.* **2012**, *32*, 2787–2798. [[CrossRef](#)]
4. Ajwad, A.; Ilyas, U.; Rashid, M.U.; Shafiq, M.I. Assessing Strengthening Techniques of Bonding overlay Concrete to Existing Concrete Elements. *NFC IEFER J. Eng. Sci. Res.* **2017**, *5*, 15–18. [[CrossRef](#)]
5. Ramírez, G.P.M.; Byliński, H.; Niedostatkiewicz, M. Deterioration and protection of concrete elements embedded in contaminated soil: A review. *Materials* **2021**, *14*, 3253. [[CrossRef](#)]
6. Safiuddin, M. Concrete damage in field conditions and protective sealer and coating systems. *Coatings* **2017**, *7*, 90. [[CrossRef](#)]
7. Sohail, M.G.; Wang, B.; Jain, A.; Kahraman, R.; Ozerkan, N.G.; Gencturk, B.; Dawood, M.; Belarbi, A. Advancements in Concrete Mix Designs: High-Performance and Ultrahigh-Performance Concretes from 1970 to 2016. *J. Mater. Civ. Eng.* **2018**, *30*, 04017310. [[CrossRef](#)]
8. Demis, S.; Papadakis, V.G. Durability design process of reinforced concrete structures—Service life estimation, problems and perspectives. *J. Build. Eng.* **2019**, *26*, 100876. [[CrossRef](#)]
9. Alexander, M.; Beushausen, H. Durability, service life prediction, and modelling for reinforced concrete structures—Review and critique. *Cem. Concr. Res.* **2019**, *122*, 17–29. [[CrossRef](#)]
10. Basheer, L.; Kropp, J.; Cleland, D.J. Assessment of the durability of concrete from its permeation properties: A review. *Constr. Build. Mater.* **2001**, *15*, 93–103. [[CrossRef](#)]
11. De Medeiros-Junior, R.A.; de Lima, M.G.; de Medeiros, M.H.F. Service life of concrete structures considering the effects of temperature and relative humidity on chloride transport. *Environ. Dev. Sustain.* **2015**, *17*, 1103–1119. [[CrossRef](#)]
12. Shi, X.; Xie, N.; Fortune, K.; Gong, J. Durability of steel reinforced concrete in chloride environments: An overview. *Constr. Build. Mater.* **2012**, *30*, 125–138. [[CrossRef](#)]
13. Val, D.V.; Stewart, M.G. Life-cycle cost analysis of reinforced concrete structures in marine environments. *Struct. Saf.* **2003**, *25*, 343–362. [[CrossRef](#)]
14. Angst, U.; Elsener, B.; Larsen, C.K.; Vennesland, Ø. Critical chloride content in reinforced concrete—A review. *Cem. Concr. Res.* **2009**, *39*, 1122–1138. [[CrossRef](#)]
15. Rodrigues, R.; Gaboreau, S.; Gance, J.; Ignatiadis, I.; Betelu, S. Reinforced concrete structures: A review of corrosion mechanisms and advances in electrical methods for corrosion monitoring. *Constr. Build. Mater.* **2021**, *269*, 121240. [[CrossRef](#)]
16. Tuutti, K. *Corrosion of Steel in Concrete*; Swedish Cement and Concrete Research Institute: Stockholm, Sweden, 1982.
17. Moser, R.D.; Singh, P.M.; Kahn, L.F.; Kurtis, K.E. Chloride-induced corrosion resistance of high-strength stainless steels in simulated alkaline and carbonated concrete pore solutions. *Corros. Sci.* **2012**, *57*, 241–253. [[CrossRef](#)]
18. Gu, P.; Elliott, S.; Beaudoin, J.J.; Arsenaault, B. Corrosion resistance of stainless steel in chloride contaminated concrete. *Cem. Concr. Res.* **1996**, *26*, 1151–1156. [[CrossRef](#)]
19. Rabi, M.; Shamass, R.; Cashell, K.A. Structural performance of stainless steel reinforced concrete members: A review. *Constr. Build. Mater.* **2022**, *325*, 126673. [[CrossRef](#)]
20. Cramer, S.D.; Covino, B.S.; Bullard, S.J.; Holcomb, G.R.; Russell, J.H.; Nelson, F.J.; Laylor, H.M.; Soltesz, S.M. Corrosion prevention and remediation strategies for reinforced concrete coastal bridges. *Cem. Concr. Compos.* **2002**, *24*, 101–117. [[CrossRef](#)]
21. Yang, D.Y.; Frangopol, D.M.; Teng, J.G. Probabilistic life-cycle optimization of durability-enhancing maintenance actions: Application to FRP strengthening planning. *Eng. Struct.* **2019**, *188*, 340–349. [[CrossRef](#)]
22. Calvet, V.; Valcuende, M.; Benlloch, J.; Cánoves, J. Influence of moderate temperatures on the bond between carbon fibre reinforced polymer bars (CFRP) and concrete. *Constr. Build. Mater.* **2015**, *94*, 589–604. [[CrossRef](#)]
23. López, F.C.-G.; Marco, J.B.; Rodríguez, V.C. Influence of high temperatures on the bond between carbon Fibre-Reinforced polymer bars and concrete. *Constr. Build. Mater.* **2021**, *309*, 124967. [[CrossRef](#)]
24. Benmokrane, B.; Wang, P.; Ton-That, T.M.; Rahman, H.; Robert, J.-F. Durability of Glass Fiber-Reinforced Polymer Reinforcing Bars in Concrete Environment. *J. Compos. Constr.* **2002**, *6*, 143–153. [[CrossRef](#)]
25. Hao, Q.; Wang, Y.; He, Z.; Ou, J. Bond strength of glass fiber reinforced polymer ribbed rebars in normal strength concrete. *Constr. Build. Mater.* **2009**, *23*, 865–871. [[CrossRef](#)]

26. Yi, Y.; Zhu, D.; Guo, S.; Zhang, Z.; Shi, C. A review on the deterioration and approaches to enhance the durability of concrete in the marine environment. *Cem. Concr. Compos.* **2020**, *113*, 103695. [[CrossRef](#)]
27. ACI 363 Report on High-Strength Concrete. 2015. Available online: https://www.academia.edu/8275753/ACI_363r_92_State_of_the_Art_Report_on_High-Strength_Concrete (accessed on 16 July 2023).
28. Faleschini, F.; Fernández-Ruiz, M.A.; Zanini, M.A.; Brunelli, K.; Pellegrino, C.; Hernández-Montes, E. High performance concrete with electric arc furnace slag as aggregate: Mechanical and durability properties. *Constr. Build. Mater.* **2015**, *101*, 113–121. [[CrossRef](#)]
29. Aitcin, P.C. The durability characteristics of high performance concrete: A review. *Cem. Concr. Compos.* **2003**, *25*, 409–420. [[CrossRef](#)]
30. Wu, K.R.; Chen, B.; Yao, W.; Zhang, D. Effect of coarse aggregate type on mechanical properties of high-performance concrete. *Cem. Concr. Res.* **2001**, *31*, 1421–1425. [[CrossRef](#)]
31. Beushausen, H.; Dittmer, T. The influence of aggregate type on the strength and elastic modulus of high strength concrete. *Constr. Build. Mater.* **2015**, *74*, 132–139. [[CrossRef](#)]
32. Kiliç, A.; Atiş, C.D.; Teymen, A.; Karahan, O.; Özcan, F.; Bilim, C.; Özdemir, M. The influence of aggregate type on the strength and abrasion resistance of high strength concrete. *Cem. Concr. Compos.* **2008**, *30*, 290–296. [[CrossRef](#)]
33. Beshr, H.; Almusallam, A.A.; Maslehuddin, M. Effect of coarse aggregate quality on the mechanical properties of high strength concrete. *Constr. Build. Mater.* **2003**, *17*, 97–103. [[CrossRef](#)]
34. Zhou, F.P.; Lydon, F.D.; Barr, B.I.G. Effect of coarse aggregate on elastic modulus and compressive strength of high performance concrete. *Cem. Concr. Res.* **1995**, *25*, 177–186. [[CrossRef](#)]
35. Bharatkumar, B.H.; Narayanan, R.; Raghuprasad, B.K.; Ramachandramurthy, D.S. Mix proportioning of high performance concrete. *Cem. Concr. Compos.* **2001**, *23*, 71–80. [[CrossRef](#)]
36. Poon, C.S.; Lam, L.; Wong, Y.L. Study on high strength concrete prepared with large volumes of low calcium fly ash. *Cem. Concr. Res.* **2000**, *30*, 447–455. [[CrossRef](#)]
37. Baroghel-Bouny, V. Conception des Bétons pour une Durée de vie Donnée des Ouvrages—Maîtrise de la Durabilité vis-à-vis de la Corrosion des Armatures et de L'alcali-Réaction—Etat de l'art et Guide pour la Mise en Oeuvre d'une Approche Performantielle et Prédictive sur la bas, Bagneux, France. 2004. Available online: <https://eprints.uanl.mx/5481/1/1020149995.PDF> (accessed on 24 July 2023).
38. Khan, M.I.; Lynsdale, C.J. Strength, permeability, and carbonation of high-performance concrete. *Cem. Concr. Res.* **2002**, *32*, 123–131. [[CrossRef](#)]
39. Shi, H.S.; Xu, B.W.; Shi, T.; Zhou, X.C. Determination of gas permeability of high performance concrete containing fly ash. *Mater. Struct. Constr.* **2008**, *41*, 1051–1056. [[CrossRef](#)]
40. Sheng, S.H.; Xu, W.B.; Zhou, X.C. Influence of mineral admixtures on compressive strength, gas permeability and carbonation of high performance concrete. *Constr. Build. Mater.* **2009**, *23*, 1980–1985. [[CrossRef](#)]
41. Zhang, X.; Zhou, X.; Zhou, H.; Gao, K.; Wang, Z. Studies on forecasting of carbonation depth of slag high performance concrete considering gas permeability. *Appl. Clay Sci.* **2013**, *79*, 36–40. [[CrossRef](#)]
42. Ozawa, M.; Sakoi, Y.; Fujimoto, K.; Tetsura, K.; Parajuli, S.S. Estimation of chloride diffusion coefficients of high-strength concrete with synthetic fibres after fire exposure. *Constr. Build. Mater.* **2017**, *143*, 322–329. [[CrossRef](#)]
43. Song, H.W.; Kwon, S.J. Evaluation of chloride penetration in high performance concrete using neural network algorithm and micro pore structure. *Cem. Concr. Res.* **2009**, *39*, 814–824. [[CrossRef](#)]
44. ASTM C1202; Standard Test Method for Electrical Indication of Concrete's Ability to Resist Chloride Ion Penetration. ASTM: West Conshohocken, PA, USA, 2012. [[CrossRef](#)]
45. NORDTEST. NT Build 492. *Rapid Chloride Migration Test (RCMT)*, Nord. Method. Nord. Coop. 1999, pp. 1–8. Available online: <https://salmanco.com/wp-content/uploads/2018/10/NT-Build-492.pdf> (accessed on 22 August 2023).
46. Shi, C.; Jiao, D.; Zhang, J.; Wang, D.; Zhang, Y.; Farzadnia, N.; Hu, X. Design of high performance concrete with multiple performance requirements for #2 Dongting Lake Bridge. *Constr. Build. Mater.* **2018**, *165*, 825–832. [[CrossRef](#)]
47. Kubissa, W.; Simon, T.; Jaskulski, R.; Reiterman, P.; Supera, M. Ecological High Performance Concrete. *Procedia Eng.* **2017**, *172*, 595–603. [[CrossRef](#)]
48. Kim, H.K.; Jang, J.G.; Choi, Y.C.; Lee, H.K. Improved chloride resistance of high-strength concrete amended with coal bottom ash for internal curing. *Comput. Chem. Eng.* **2014**, *71*, 334–343. [[CrossRef](#)]
49. Gonzalez-Corominas, A.; Etxeberria, M.; Poon, C.S. Influence of steam curing on the pore structures and mechanical properties of fly-ash high performance concrete prepared with recycled aggregates. *Cem. Concr. Compos.* **2016**, *71*, 77–84. [[CrossRef](#)]
50. Akca, A.H.; Zihnio, N.Ö. High performance concrete under elevated temperatures. *Constr. Build. Mater.* **2013**, *44*, 317–328. [[CrossRef](#)]
51. Noumowe, A.N.; Siddique, R.; Debicki, G. Permeability of high-performance concrete subjected to elevated temperature (600 °C). *Constr. Build. Mater.* **2009**, *23*, 1855–1861. [[CrossRef](#)]
52. Chan, Y.N.; Peng, G.F.; Anson, M. Residual strength and pore structure of high-strength concrete and normal strength concrete after exposure to high temperatures. *Cem. Concr. Compos.* **1999**, *21*, 23–27. [[CrossRef](#)]
53. Chan, Y.N.; Luo, X.; Sun, W. Compressive strength and pore structure of highperformance concrete (chan). *Cem. Concr. Res.* **2000**, *30*, 247–251. [[CrossRef](#)]

54. Gonzalez-Corominas, A.; Etxeberria, M. Effects of using recycled concrete aggregates on the shrinkage of high performance concrete. *Constr. Build. Mater.* **2016**, *115*, 32–41. [[CrossRef](#)]
55. Tayeh, B.A.; Saffar, D.M.A.; Alyousef, R. The Utilization of Recycled Aggregate in High Performance Concrete: A Review. *J. Mater. Res. Technol.* **2020**, *9*, 8469–8481. [[CrossRef](#)]
56. Huang, H.; Gao, X.; Wang, H.; Ye, H. Influence of rice husk ash on strength and permeability of ultra-high performance concrete. *Constr. Build. Mater.* **2017**, *149*, 621–628. [[CrossRef](#)]
57. Zhang, M.H.; Malhotra, V.M. High-performance concrete incorporating rice husk ash as a supplementary cementing material. *ACI Mater. J.* **1996**, *93*, 629–636. [[CrossRef](#)]
58. Cordeiro, G.C.; Filho, R.D.T.; De Moraes, R.F.E. Use of ultrafine rice husk ash with high-carbon content as pozzolan in high performance concrete. *Mater. Struct. Constr.* **2009**, *42*, 983–992. [[CrossRef](#)]
59. Alkhatib, A.; Maslehuddin, M.; Al-Dulaijan, S.U. Development of high performance concrete using industrial waste materials and nano-silica. *J. Mater. Res. Technol.* **2020**, *9*, 6696–6711. [[CrossRef](#)]
60. Suzuki, M.; Meddah, M.S.; Sato, R. Use of porous ceramic waste aggregates for internal curing of high-performance concrete. *Cem. Concr. Res.* **2009**, *39*, 373–381. [[CrossRef](#)]
61. Larrard, F.; Sedran, T. Optimization of ultra-high-performance concrete by the use of a packing model. *Cem. Concr. Res.* **1994**, *24*, 997–1009. [[CrossRef](#)]
62. Camacho Torregrosa, E. Dosage Optimization and Bolted Connections for UHPFRC Ties. Dosage Optimization and Bolted Connections for UHPFRC. Ph.D. Thesis, Universitat Politècnica de València, Valencia, Spain, 2013. Available online: <https://riUNET.upv.es/handle/10251/34790?show=full> (accessed on 11 July 2023).
63. AFGC/SETRA Groupe de Travail BFUP. *Bétons Fibrés à Ultra-Hautes Performances*; ACI: Farmington Hills, MI, USA, 2002. [[CrossRef](#)]
64. Resplendino, J. Ultra High Performance Concrete: New AFGC Recommendations. *Des. Build. UHPFRC* **2013**, *10*, 713–722. [[CrossRef](#)]
65. Azmee, N.M.; Shafiq, N. Ultra-high performance concrete: From fundamental to applications. *Case Stud. Constr. Mater.* **2018**, *9*, e00197. [[CrossRef](#)]
66. Kansal, C.M.; Goyal, R. Effect of nano silica, silica fume and steel slag on concrete properties. *Mater. Today Proc.* **2021**, *45*, 4535–4540. [[CrossRef](#)]
67. Xi, J.; Liu, J.; Yang, K.; Zhang, S.; Han, F.; Sha, J.; Zheng, X. Role of silica fume on hydration and strength development of ultra-high performance concrete. *Constr. Build. Mater.* **2022**, *338*, 127600. [[CrossRef](#)]
68. Xiong, X.; Wu, M.; Shen, W.; Li, J.; Zhao, D.; Li, P.; Wu, J. Performance and microstructure of ultra-high-performance concrete (UHPC) with silica fume replaced by inert mineral powders. *Constr. Build. Mater.* **2022**, *327*, 126996. [[CrossRef](#)]
69. Ha, N.S.; Marundrury, S.S.; Pham, T.M.; Pournasiri, E.; Shi, F.; Hao, H. Effect of grounded blast furnace slag and rice husk ash on performance of ultra-high-performance concrete (UHPC) subjected to impact loading. *Constr. Build. Mater.* **2022**, *329*, 127213. [[CrossRef](#)]
70. Pyo, S.; Kim, H.K. Fresh and hardened properties of ultra-high performance concrete incorporating coal bottom ash and slag powder. *Constr. Build. Mater.* **2017**, *131*, 459–466. [[CrossRef](#)]
71. Roux, N.; Andrade, C.; Sanjuan, M.A. Experimental Study of Durability of Reactive Powder Concretes. *J. Mater. Civ. Eng.* **1996**, *8*, 1–6. [[CrossRef](#)]
72. Du, J.; Liu, Z.; Christodoulatos, C.; Conway, M.; Bao, Y.; Meng, W. Utilization of off-specification fly ash in preparing ultra-high-performance concrete (UHPC): Mixture design, characterization, and life-cycle assessment. *Resour. Conserv. Recycl.* **2022**, *180*, 106136. [[CrossRef](#)]
73. Mostafa, S.A.; EL-Deeb, M.M.; Farghali, A.A.; Fariad, A.S. Evaluation of the nano silica and nano waste materials on the corrosion protection of high strength steel embedded in ultra-high performance concrete. *Sci. Rep.* **2021**, *11*, 2617. [[CrossRef](#)]
74. Liu, Y.; Jing, R.; Yan, P. Improving environmental efficiency of ultra-high-performance concrete (UHPC) through appropriate application of ultrafine quartz powder. *J. Sustain. Cem. Mater.* **2022**, *2022*, 21650373. [[CrossRef](#)]
75. Soliman, N.A.; Tagnit-Hamou, A. Partial substitution of silica fume with fine glass powder in UHPC: Filling the micro gap. *Constr. Build. Mater.* **2017**, *139*, 374–383. [[CrossRef](#)]
76. Omran, A.; Tagnit-Hamou, A. Performance of glass-powder concrete in field applications. *Constr. Build. Mater.* **2016**, *109*, 84–95. [[CrossRef](#)]
77. Valcuende, M.; Lliso-Ferrando, J.R.; Roig-Flores, M.; Gandía-Romero, J.M. Porous Structure of ultra-high-performance fibre-reinforced concretes. *Materials* **2021**, *14*, 1637. [[CrossRef](#)]
78. Van Tuan, N.; Ye, G.; Van Breugel, K.; Copuroglu, O. Hydration and microstructure of ultra high performance concrete incorporating rice husk ash. *Cem. Concr. Res.* **2011**, *41*, 1104–1111. [[CrossRef](#)]
79. Abdulkareem, O.M.; Fraj, A.B.; Bouasker, M.; Khouchaf, L.; Khelidj, A. Microstructural investigation of slag-blended UHPC: The effects of slag content and chemical/thermal activation. *Constr. Build. Mater.* **2021**, *292*, 123455. [[CrossRef](#)]
80. Vernet, C.P. Ultra-Durable Concretes: Structure at the Micro- and Nanoscale. *MRS Bull.* **2004**, *29*, 324–327. [[CrossRef](#)]
81. Abbas, S.; Nehdi, M.L.; Saleem, M.A. Ultra-High Performance Concrete: Mechanical Performance, Durability, Sustainability and Implementation Challenges. *Int. J. Concr. Struct. Mater.* **2016**, *10*, 271–295. [[CrossRef](#)]

82. Cheyrezy, M.; Maret, V.; Frouin, L. Microstructural analysis of RPC (Reactive Powder Concrete). *Cem. Concr. Res.* **1995**, *25*, 1491–1500. [[CrossRef](#)]
83. Wang, R.; Gao, X.; Li, Q.; Yang, Y. Influence of splitting load on transport properties of ultra-high performance concrete. *Constr. Build. Mater.* **2018**, *171*, 708–718. [[CrossRef](#)]
84. Tafraoui, A.; Escadeillas, G.; Vidal, T. Durability of the Ultra High Performances Concrete containing metakaolin. *Constr. Build. Mater.* **2016**, *112*, 980–987. [[CrossRef](#)]
85. Ghafari, E.; Costa, H.; Júlio, E.; Portugal, A.; Durães, L. The effect of nanosilica addition on flowability, strength and transport properties of ultra high performance concrete. *Mater. Des.* **2014**, *59*, 1–9. [[CrossRef](#)]
86. Matos, A.M.; Nunes, S.; Costa, C.; Barroso-Aguiar, J.L. Characterization of Non-proprietary UHPC for Use in Rehabilitation/Strengthening Applications. In *Rheology and Processing of Construction Materials: RheoCon2 & SCC9 2*; Springer: Berlin/Heidelberg, Germany, 2020; pp. 554–559. [[CrossRef](#)]
87. Jaafar, M.F.M.; Saman, H.M.; Sidek, M.N.M.; Muthusamy, K.; Ismail, N. Performance of nano metaclay on chloride diffusion for ultra- high performance concrete. *IOP Conf. Ser. Earth Environ. Sci.* **2021**, *682*, 012002. [[CrossRef](#)]
88. Qian, Y.; Yang, D.; Xia, Y.; Gao, H.; Ma, Z. Transport Properties and Resistance Improvement of Ultra-High Performance Concrete (UHPC) after Exposure to Elevated Temperatures. *Buildings* **2021**, *11*, 416. [[CrossRef](#)]
89. Matos, A.M.; Nunes, S.; Costa, C.; Aguiar, J.L.B. Durability of an UHPC containing spent equilibrium catalyst. *Constr. Build. Mater.* **2021**, *305*, 124681. [[CrossRef](#)]
90. Luan, C.; Wang, J.; Gao, J.; Wang, J.; Du, P.; Zhou, Z.; Huang, Y.; Du, S. Changes in fractal dimension and durability of ultra-high performance concrete (UHPC) with silica fume content. *Arch. Civ. Mech. Eng.* **2022**, *22*, 123. [[CrossRef](#)]
91. Wang, D.; Shi, C.; Wu, Z.; Xiao, J.; Huang, Z.; Fang, Z. A review on ultra high performance concrete: Part II. Hydration, microstructure and properties. *Constr. Build. Mater.* **2015**, *96*, 368–377. [[CrossRef](#)]
92. Sharma, R.; Jang, J.G.; Bansal, P.P. A comprehensive review on effects of mineral admixtures and fibers on engineering properties of ultra-high-performance concrete. *J. Build. Eng.* **2022**, *45*, 103314. [[CrossRef](#)]
93. Du, Y.; Qi, H.H.; Huang, S.S.; Liew, J.Y.R. Experimental study on the spalling behaviour of ultra-high strength concrete in fire. *Constr. Build. Mater.* **2020**, *258*, 120334. [[CrossRef](#)]
94. Graybeal, B.; Tanesi, J. A cementitious long-life wearing course to reduce frequency of maintenance works on high-traffic roads. *Transp. Res. Arena Eur.* **2008**, *1561*, 454–461.
95. Mousavi, S.M.; Ranjbar, M.M.; Madandoust, R. Combined effects of steel fibers and water to cementitious materials ratio on the fracture behavior and brittleness of high strength concrete. *Eng. Fract. Mech.* **2019**, *216*, 106517. [[CrossRef](#)]
96. Şahin, Y.; Köksal, F. The influences of matrix and steel fibre tensile strengths on the fracture energy of high-strength concrete. *Constr. Build. Mater.* **2011**, *25*, 1801–1806. [[CrossRef](#)]
97. Shi, C.; Wu, Z.; Xiao, J.; Wang, D.; Huang, Z.; Fang, Z. A review on ultra high performance concrete: Part I. Raw materials and mixture design. *Constr. Build. Mater.* **2015**, *101*, 741–751. [[CrossRef](#)]
98. Hassan, A.M.T.; Jones, S.W.; Mahmud, G.H. Experimental test methods to determine the uniaxial tensile and compressive behaviour of Ultra High Performance Fibre Reinforced Concrete(UHPFRC). *Constr. Build. Mater.* **2012**, *37*, 874–882. [[CrossRef](#)]
99. Máca, P.; Sovják, R.; Vavříník, T. Experimental investigation of mechanical properties of UHPFRC. *Procedia Eng.* **2013**, *65*, 14–19. [[CrossRef](#)]
100. Máca, P.; Sovják, R.; Konvalinka, P. Mix design of UHPFRC and its response to projectile impact. *Int. J. Impact Eng.* **2014**, *63*, 158–163. [[CrossRef](#)]
101. Kusumawardaningsih, Y.; Fehling, E.; Ismail, M. UHPC compressive strength test specimens: Cylinder or cube? *Procedia Eng.* **2015**, *125*, 1076–1080. [[CrossRef](#)]
102. Valcuende, M.; Lliso-Ferrando, J.R.; Ramón-Zamora, J.E.; Soto, J. Corrosion resistance of ultra-high performance fibre-reinforced concrete. *Constr. Build. Mater.* **2021**, *306*, 124914. [[CrossRef](#)]
103. Tayeh, B.A.; Aadi, A.S.; Hilal, N.N.; Bakar, B.H.A.; Al-Tayeb, M.M.; Mansour, W.N. Properties of ultra-high-performance fiber-reinforced concrete (UHPFRC)—A review paper. *AIP Conf. Proc.* **2019**, *1*, 2157. [[CrossRef](#)]
104. Yang, J.; Chen, B.; Su, J.; Xu, G.; Zhang, D.; Zhou, J. Effects of fibers on the mechanical properties of UHPC: A review. *J. Traffic Transp. Eng.* **2022**, *9*, 363–387. [[CrossRef](#)]
105. Kang, S.T.; Lee, Y.; Park, Y.D.; Kim, J.K. Tensile fracture properties of an Ultra High Performance Fiber Reinforced Concrete (UHPFRC) with steel fiber. *Compos. Struct.* **2010**, *92*, 61–71. [[CrossRef](#)]
106. Ghafari, E.; Costa, H.; Júlio, E.; Portugal, A.; Duraes, L. Optimization of UHPC by Adding Nanomaterials. In Proceedings of the 3rd International Symposium on UHPC and Nanotechnology for High Performance Construction Materials, Kassel, Germany, 7–9 March 2012.
107. Abushanab, A.; Alnahhal, W.; Sohail, M.G.; Alnuaimi, N.; Kahraman, R.; Altayeh, N. Mechanical and durability properties of ultra-high performance steel FRC made with discarded materials. *J. Build. Eng.* **2021**, *44*, 103264. [[CrossRef](#)]
108. Hannawi, K.; Bian, H.; Prince-Agbojjan, W.; Raghavan, B. Effect of different types of fibers on the microstructure and the mechanical behavior of Ultra-High Performance Fiber-Reinforced Concretes. *Compos. Part B Eng.* **2016**, *86*, 214–220. [[CrossRef](#)]
109. Wang, W.; Liu, J.; Agostini, F.; Davy, C.A.; Skoczylas, F.; Corvez, D. Durability of an Ultra High Performance Fiber Reinforced Concrete (UHPFRC) under progressive aging. *Cem. Concr. Res.* **2014**, *55*, 1–13. [[CrossRef](#)]

110. Li, Y.; Pimienta, P.; Pinoteau, N.; Tan, K.H. Effect of aggregate size and inclusion of polypropylene and steel fibers on explosive spalling and pore pressure in ultra-high-performance concrete (UHPC) at elevated temperature. *Cem. Concr. Compos.* **2019**, *99*, 62–71. [[CrossRef](#)]
111. Kewalramani, M.; Khartabil, A. Porosity evaluation of concrete containing supplementary cementitious materials for durability assessment through volume of permeable voids and water immersion conditions. *Buildings* **2021**, *11*, 378. [[CrossRef](#)]
112. Martínez-Ibernón, A.; Roig-Flores, M.; Lliso-Ferrando, J.; Mezquida-Alcaraz, E.J.; Valcuende, M.; Serna, P. Influence of cracking on oxygen transport in UHPFRC using stainless steel sensors. *Appl. Sci.* **2020**, *10*, 239. [[CrossRef](#)]
113. *UNE 83980:2014*; Determinación de la Absorción de Agua, la Densidad y la Porosidad Accesible al Agua del Hormigón. AENOR: Madrid, Spain, 2014.
114. *UNE 83982:2008*; Determinación de la Absorción de Agua por Capilaridad del Hormigón Endurecido. AENOR: Madrid, Spain, 2008.
115. *UNE 83966:2008*; Acondicionamiento de Probetas de Hormigón para los Ensayos de Permeabilidad a Gases y Capilaridad. AENOR: Madrid, Spain, 2008.
116. *UNE 83981:2008*; Determinación de la Permeabilidad al Oxígeno del Hormigón Endurecido. AENOR: Madrid, Spain, 2008.
117. *UNE-EN 12390-18:2021*; Determinación del Coeficiente de Migración de Cloruros. AENOR: Madrid, Spain, 2021.
118. *UNE-EN 12390-11:2019*; Determinación de la Resistencia a los Cloruros del Hormigón, Difusión Unidireccional. AENOR: Madrid, Spain, 2019.
119. *UNE-EN 14629:2007*; Determinación del contenido de cloruros en el hormigón endurecido. AENOR: Madrid, Spain, 2007.
120. Gowers, K.; Millard, S. Measurement of Concrete Resistivity for Assessment of Corrosion. *ACI Mater. J.* **1999**, *96*, 536–541.
121. Azarsa, P.; Gupta, R. Resistivity of Concrete for Electrical Durability Evaluation: A Review. *Adv. Mater. Sci. Eng.* **2017**, *2017*, 8453095. [[CrossRef](#)]
122. Gulikers, J. Theoretical considerations on the supposed linear relationship between concrete resistivity and corrosion rate of steel reinforcement. *Mater. Corros.* **2005**, *56*, 393–403. [[CrossRef](#)]
123. *UNE 83988-1:2008*; Determinación de la Resistividad Eléctrica. Método Directo. AENOR: Madrid, Spain, 2008.
124. Kreijger, P.C. The skin of concrete composition and properties. *Matériaux Constr.* **1984**, *17*, 275–283. [[CrossRef](#)]
125. Aïssoun, B.M.; Gallias, J.L.; Khayat, K.H. Influence of formwork material on transport properties of self-consolidating concrete near formed surfaces. *Constr. Build. Mater.* **2017**, *146*, 329–337. [[CrossRef](#)]
126. *D1141-98*; Standard Practice for the Preparation of Substitute Ocean Water. ASTM: West Conshohocken, PA, USA, 2021.
127. Ramón, J.E.; Martínez-Ibernón, A.; Gandía-Romero, J.M.; Fraile, R.; Bataller, R.; Alcañiz, M.; García-Breijo, E.; Soto, J. Characterization of electrochemical systems using potential step voltammetry. Part I: Modeling by means of equivalent circuits. *Electrochim. Acta* **2019**, *323*, 134702. [[CrossRef](#)]
128. Ramón, J.E.; Gandía-Romero, J.M.; Bataller, R.; Alcañiz, M.; Valcuende, M.; Soto, J. Potential step voltammetry: An approach to corrosion rate measurement of reinforcements in concrete. *Cem. Concr. Compos.* **2020**, *110*, 103590. [[CrossRef](#)]
129. Martínez-Ibernón, A.; Ramón, J.E.; Gandía-Romero, J.M.; Gasch, I.; Valcuende, M.; Alcañiz, M.; Soto, J. Characterization of electrochemical systems using potential step voltammetry. Part II: Modeling of reversible systems. *Electrochim. Acta* **2019**, *328*, 135111. [[CrossRef](#)]
130. Ramón, J.E.; Martínez, I.; Gandía-Romero, J.M.; Soto, J. Improved Tafel-Based Potentiostatic Approach for Corrosion Rate Monitoring of Reinforcing Steel. *J. Nondestruct. Eval.* **2022**, *41*, 70. [[CrossRef](#)]
131. Lliso-Ferrando, J.R. *Monitorización de la Durabilidad de Estructuras Existentes de Hormigón Armado Mediante la Inserción de una Red de Sensores*; Universitat Politècnica de València: Valencia, Spain, 2022.
132. Lliso-Ferrando, J.R.; Gasch, I.; Martínez-Ibernón, A.; Valcuende, M. Effect of macrocell currents on rebar corrosion in reinforced concrete structures exposed to a marine environment. *Ocean Eng.* **2022**, *257*, 111680. [[CrossRef](#)]
133. Ramón, J.E.; Gandía-Romero, J.M.; Bataller, R.; López, J.A.; Valcuende, M.; Soto, J. Real-time corrosion monitoring of an ultra-high performance fibre-reinforced concrete offshore raft by using an autonomous sensor system. *Struct. Control Health Monit.* **2022**, *29*, e3102. [[CrossRef](#)]
134. Siddique, R. Utilization of silica fume in concrete: Review of hardened properties. *Resour. Conserv. Recycl.* **2011**, *55*, 923–932. [[CrossRef](#)]
135. Poon, C.S.; Kou, S.C.; Lam, L. Compressive strength, chloride diffusivity and pore structure of high performance metakaolin and silica fume concrete. *Constr. Build. Mater.* **2006**, *20*, 858–865. [[CrossRef](#)]
136. Chinchillas-Chinchillas, M.J.; Rosas-Casarez, C.A.; Arredondo-Rea, S.P.; Gómez-Soberón, J.M.; Corral-Higuera, R. SEM image analysis in permeable recycled concretes with silica fume. A quantitative comparison of porosity and the ITZ. *Materials* **2019**, *12*, 2201. [[CrossRef](#)]
137. Kupwade-Patil, K.; Palkovic, S.D.; Bumajdad, A.; Soriano, C.; Büyüköztürk, O. Use of silica fume and natural volcanic ash as a replacement to Portland cement: Micro and pore structural investigation using NMR, XRD, FTIR and X-ray microtomography. *Constr. Build. Mater.* **2018**, *158*, 574–590. [[CrossRef](#)]
138. AFGC/SETRA Groupe de Travail BFUP. Betons fibres a ultra-hautes performances Ultra High Performance Fibre-Reinforced Concretes. Recommendations. *Doc. Sci. Tech.* **2013**, 359. Available online: <https://www.afgc.asso.fr/app/uploads/2007/10/Recommandations-BFUP-Juin-2013.pdf> (accessed on 21 June 2023).

139. Andrade, C.; Bettencourt-Ribeiro, A.; Buenfeld, R.; Carcasses, M.; Carino, N.J.; Ehrenberg, F.; Ewestson, C.; Garboczi, E.; Geiker, M.; Gjørsv, O.E.; et al. RILEM TC 116-PCD: Permeability of Concrete as a Criterion of its Durability. Determination of the Capillary Absorption of Water of Hardened Concrete. *Mater. Struct.* **1999**, *32*, 174–179.
140. Hooton, D.; Pun, P. Influence of silica fume on chloride resistance of concrete. In *Proquest Information and Learning*; SFA: Dover, DE, USA, 2014.
141. Byfors, K. Influence of silica fume and fly ash on chloride diffusion and pH values in cement paste. *Cem. Concr. Res.* **1987**, *17*, 115–130. [[CrossRef](#)]
142. Torii, K.; Kawamura, M. Pore structure and chloride ion permeability of mortars containing silica fume. *Cem. Concr. Compos.* **1994**, *16*, 279–286. [[CrossRef](#)]
143. Bentz, D.P.; Jensen, O.M.; Coats, A.M.; Glasser, F.P. Influence of silica fume on diffusivity in cement-based materials. I. Experimental and computer modeling studies on cement pastes. *Cem. Concr. Res.* **2000**, *30*, 953–962. [[CrossRef](#)]
144. Jensen, O.M. Chloride ingress in cement paste and mortar measured by Electron Probe Micro Analysis. *Dep. Struct. Eng. Mater.* **1999**, *63*, 58–60.
145. Teng, S.; Afroughsabet, V.; Ostertag, C.P. Flexural behavior and durability properties of high performance hybrid-fiber-reinforced concrete. *Constr. Build. Mater.* **2018**, *182*, 504–515. [[CrossRef](#)]
146. Pourjahanshahi, A.; Madani, H. Chloride diffusivity and mechanical performance of UHPC with hybrid fibers under heat treatment regime. *Mater. Today Commun.* **2021**, *26*, 102146. [[CrossRef](#)]
147. Frazão, C.; Camões, A.; Barros, J.; Gonçalves, D. Durability of steel fiber reinforced self-compacting concrete. *Constr. Build. Mater.* **2015**, *80*, 155–166. [[CrossRef](#)]
148. Fan, L.; Meng, W.; Teng, L.; Khayat, K.H. Effects of lightweight sand and steel fiber contents on the corrosion performance of steel rebar embedded in UHPC. *Constr. Build. Mater.* **2020**, *238*, 117709. [[CrossRef](#)]
149. Afroughsabet, V.; Biolzi, L.; Monteiro, P.J.M. The effect of steel and polypropylene fibers on the chloride diffusivity and drying shrinkage of high-strength concrete. *Compos. Part B Eng.* **2018**, *139*, 84–96. [[CrossRef](#)]
150. El-Dieb, A.S. Mechanical, durability and microstructural characteristics of ultra-high-strength self-compacting concrete incorporating steel fibers. *Mater. Des.* **2009**, *30*, 4286–4292. [[CrossRef](#)]
151. Chen, Y.; Matalkah, F.; Weerasiri, R.R.; Balachandra, A. Dispersion of Fibers in Ultra-High-Performance Concrete. *Concr. Int.* **2017**, *39*, 45–50.
152. Yoo, D.Y.; Kim, S.W.; Park, J.J. Comparative flexural behavior of ultra-high-performance concrete reinforced with hybrid straight steel fibers. *Constr. Build. Mater.* **2017**, *132*, 219–229. [[CrossRef](#)]
153. Kim, J.J.; Jang, Y.S.; Yoo, D.Y. Enhancing the tensile performance of ultra-high-performance concrete through novel curvilinear steel fibers. *J. Mater. Res. Technol.* **2020**, *9*, 7570–7582. [[CrossRef](#)]
154. Zhang, J.; Wang, J.; Kong, D. Chloride diffusivity analysis of existing concrete based on Fick's second law. *J. Wuhan Univ. Technol. Mater. Sci. Ed.* **2010**, *25*, 142–146. [[CrossRef](#)]
155. Mangat, P.S.; Molloy, B.T. Prediction of long term chloride concentration in concrete. *Mater. Struct.* **1994**, *27*, 338–346. [[CrossRef](#)]
156. Ma, J.; Lin, P. Simulation Approach for Random Diffusion of Chloride in Concrete under Sustained Load with Cellular Automata. *Materials* **2022**, *15*, 4384. [[CrossRef](#)] [[PubMed](#)]
157. Andrade, C. Concepts on the chloride diffusion coefficient. In Proceedings of the Third RILEM Workshop on Testing and Modelling the Chloride Ingress into Concrete, Madrid, Spain, 9–10 September 2002. [[CrossRef](#)]
158. Cao, Y.; Gehlen, C.; Angst, U.; Wang, L.; Wang, Z.; Yao, Y. Critical chloride content in reinforced concrete—An updated review considering Chinese experience. *Cem. Concr. Res.* **2019**, *117*, 58–68. [[CrossRef](#)]
159. Tang, L.; Utgenannt, P. A field study of critical chloride content in reinforced concrete with blended binder. *Mater. Corros.* **2009**, *60*, 617–622. [[CrossRef](#)]
160. Martinie, L.; Lataste, J.F.; Roussel, N. Fiber orientation during casting of UHPFRC: Electrical resistivity measurements, image analysis and numerical simulations. *Mater. Struct. Constr.* **2015**, *48*, 947–957. [[CrossRef](#)]
161. UNE 112072:2011; Determinación de la Velocidad de Corrosión de Armaduras en Laboratorio Mediante Medida de la Resistencia a la Polarización. AENOR: Madrid, Spain, 2011.
162. ASTM G1-03; Standard Practice for Preparing, Cleaning, and Evaluating Corrosion Test Specimens. American Society of Testing Materials (ASTM): West Conshohocken, PA, USA, 1999.

Disclaimer/Publisher's Note: The statements, opinions and data contained in all publications are solely those of the individual author(s) and contributor(s) and not of MDPI and/or the editor(s). MDPI and/or the editor(s) disclaim responsibility for any injury to people or property resulting from any ideas, methods, instructions or products referred to in the content.